

Mean-Motion Resonances With Interfering Density Waves

Huan Yang^{1,2,3*} Ya-Ping Li^{4†}

¹*Department of Astronomy, Tsinghua University, Beijing 100084, China*

²*Perimeter Institute for Theoretical Physics, Waterloo, ON N2L2Y5, Canada*

³*University of Guelph, Guelph, Ontario N1G 2W1, Canada*

⁴*Shanghai Astronomical Observatory, Chinese Academy of Sciences, Shanghai 200030, People's Republic of China*

Accepted XXX. Received YYY; in original form ZZZ

ABSTRACT

In this work, we study the dynamics of two less massive objects moving around a central massive object, which are all embedded within a thin accretion disc. In addition to the gravitational interaction between these objects, the disc-object interaction is also crucial for describing the long-term dynamics of the multi-body system, especially in the regime of mean-motion resonances. We point out that near the resonance the density waves generated by the two moving objects generally coherently interfere with each other, giving rise to extra angular momentum fluxes. The resulting backreaction on the objects is derived within the thin-disc scenario, which explicitly depends on the resonant angle and sensitively depends on the smoothing scheme used in the two-dimensional theory. We have performed hydrodynamical simulations with planets embedded within a thin accretion disc and have found qualitative agreement on the signatures of interfering density waves by measuring the torques on the embedded objects, for the cases of 2 : 1 and 3 : 2 resonance. By including in interference torque and the migration torques in the evolution of a pair of planets, we show that the chance of resonance trapping depends on the sign of the interference torque. For negative interference torques the pairs are more likely located at off-resonance regimes. The negative interference torques may also explain the 1% – 2% offset (for the period ratios) from the exact resonance values as observed in *Kepler* multi-planet systems.

Key words: accretion, accretion discs – Planetary Systems – gravitational waves – planets and satellites: dynamical evolution and stability

1 INTRODUCTION

Mean motion resonances (MMRs) generally arise for a system with two (or more) point masses orbiting around a common massive object. The mutual gravitational interaction between the two point masses gives rise to resonant dynamics of the resonant degree of freedom of this system when the period ratio is close to $j + k : j$ (Murray & Dermott 2000), where both j, k are integers. This general setting applies for various astrophysical systems at different scales, including satellites orbiting around planets (Peale 1976), planets orbiting around stars (Petrovich et al. 2013), and stars/stellar-mass black holes orbiting around supermassive black holes (Yang et al. 2019; Peng & Chen 2023). For example, it is known that the satellites Mimas and Tethys of Saturn are in a 4 : 2 resonance with their mean motions being $n_M : n_{Te} = 2.003139$ (Murray & Dermott 2000). The *Kepler* mission has detected thousands of planets, some of which (although much less than expected) belong to multi-planet systems that exhibit resonant period ratios as well (Lissauer et al. 2012; Fabrycky

et al. 2014; Weiss et al. 2022; Huang & Ormel 2023; Dai et al. 2024). On the other hand, the AGN (Active Galactic Nuclei) may capture stellar-mass black holes from the nuclear star cluster through the density wave generation (Tanaka et al. 2002; Tanaka & Ward 2004). The embedded stellar-mass black holes may be gravitationally captured into binaries within the AGN disc (Li et al. 2023; DeLaurentiis et al. 2023; Rowan et al. 2023, 2024; Wang et al. 2024; Whitehead et al. 2024), which subsequently become sources for ground-based gravitational wave detectors (e.g., Li et al. 2021, 2022; Dempsey et al. 2022; Kaaz et al. 2023; Li & Lai 2022, 2023; Lai & Muñoz 2023). They may also migrate towards the central massive black hole and eventually become extreme mass-ratio inspirals (EMRIs), which is expected to be an important or even dominant EMRI source for space-borne gravitational wave detectors (Pan & Yang 2021a; Pan et al. 2021; Pan & Yang 2021b). If a pair of stellar-mass black holes are trapped into an MMR, they may migrate together towards the central massive black hole for certain period of time until the resonance locking breaks down (Yang et al. 2019; Peng & Chen 2023). This possibly lead to subsequent EMRI events from the same galaxy with relatively short separations and/or gravitational environmental impacts on the EMRI waveform

* E-mail: hyangdoa@tsinghua.edu.cn

† E-mail: liyp@shao.ac.cn

due to the tidal resonance effect (Bonga et al. 2019; Pan et al. 2023).

Starting from an initial state away from the MMR, a system may be captured into resonance due to additional dissipation mechanisms, i.e., migration torques from the disc. The probability of resonance capture depends on factors such as the migration direction, the initial orbital eccentricity, the masses of planets and central stars, etc (Murray & Dermott 2000). In addition, Goldreich & Schlichting (2014) (hereafter GS14) showed that by incorporating migration torques into the long-term evolution of a pair of planets orbiting around a star, it is possible to explain that *Kepler* has observed much less than 50% multi-planet systems trapped into MMRs¹. The period ratios for those residing near resonances are slightly larger than the exact resonances values, which is consistent with the requirement that resonance capture requires convergent migration. However, the average 1% – 2% offset from the exact resonance values for the period ratios is difficult to explain within the framework of GS14, so that it was conjectured additional mechanism is in operation to deduce the eccentricity and enhance the period ratio offset. There are debated arguments about whether tidal damping can account for the increased period ratio offset (Lithwick & Wu 2012; Batygin & Morbidelli 2013; Lee et al. 2013). It has also been suggested that dissipation of density waves near the planets may reverse the migration direction and/or increase the period ratio offset. It is however also worth to note that such mechanism is likely more relevant for massive planets with gap opening on the proto-planetary discs (Baruteau & Papaloizou 2013).

We notice that when there are multiple planets moving within a disc, the total density wave generated will be a superposition of waves contributed by each planet. In cases where planet orbital frequencies are not commensurate, the interference between different components of density waves only produce an oscillatory flux that averages to zero in time. So it is reasonable to expect to no secular effect associated with interfering density waves in this regime. However, when the planets are trapped in the resonance regime the density waves may stay in phase for an extended period of time so that their interference gives rise to additional angular momentum fluxes. The backreaction should also modify the resonant dynamics of the pair of planets.

In this work we explicitly compute the backreaction on the planets in resonant due to interfering density waves assuming a thin-disc scenario. Using a two-dimensional disc perturbation theory along with a vertical smoothing scheme, we find that the backreaction torque is a sinusoidal function of the resonant phase angle as analogous to the mutual gravitational interactions. The torque is mainly produced in the regime where the location of a Lindblad resonance overlaps with the orbit of a planet. We find that the sign and magnitude of the torque, however, sensitively depends on the different smoothing schemes used in the two-dimensional theory. This means that the physical torque has to be computed in the three-dimensional setup. In order to further test the pre-

dictions of theory, we further carry out two-dimensional hydrodynamic simulations of these star+planets+disc systems using the FARGO3D code (Benítez-Llambay & Masset 2016). By performing the simulations with a pair of planets and with individual planet, we can extract the additional torque due to the interference effect for the cases of 2 : 1 and 3 : 2 resonance. The result qualitatively agrees with the analytical in terms of the location of the peak torque density, the sign of the torque, with a factor of a few difference in the magnitude, which possibly comes from the approximation made in the analytical theory.

With the interference torque included in the orbital evolution of a pair of planets, we find that a positive interference torque (that tends to drive the inner planet outward) generally leads to higher chance of resonance locking, whereas a negative torque tends to produce more pairs of planets with period ratio away from the resonant values. This is interestingly consistent with the fact that the majority of *Kepler*'s planet pairs are found away from resonant period ratios. We further examine the co-evolution of planet pairs with similar set-ups in GS14, in connection to *Kepler* observations. We find that for the same sets of planets and disc profiles, the interfering density wave terms are able to boost the period ratio offset by more than a factor of four, so that the observed offset level $\sim 1\% - 2\%$ is much more compatible with the phenomenological evolution model discussed in GS14. Therefore the interfering density waves likely play an important role in the morphology of astrophysical multi-planet systems.

This paper is organized as follows. In Sec. 2 we perform an analytical calculation of the backreaction torque acting on planets due to the interfering density waves, under the thin-disc approximation. We further derive the consequent effect on the change rate of orbital eccentricity and frequency. In Sec. 3 we carry out hydrodynamical simulations of the multi-planet systems embedded within an accretion disc to test the theory of interfering density waves. In Sec. 4 we discuss the modified resonant dynamics due to the interfering density waves, with or without considering the migration torques. In Sec. 5 we discuss the observational signatures of the interfering density waves in connection to the *Kepler* observations. We conclude in Sec. 6.

2 INTERFERING DENSITY WAVES AND THEIR BACKREACTION

Let us consider multiple objects moving within a thin disc, the gravitational fields of which excite density waves through the Lindblad resonance and the corotation resonance. Density waves carry away energy and angular momentum, which in turn lead to backreaction on the objects as migration torques. These density waves generally have different frequencies as sourced by individual objects, so that the interaction between one object and density waves generated by other objects should be oscillatory, i.e., no secular effect in the long-term evolution. On the other hand, it has been pointed out that density waves may be damped at co-orbital regions of the objects due to dissipation of shocks (Podlewska-Gaca et al. 2012), so that these objects receive additional secular torques by dissipative interaction with density waves. This mechanism is efficient if one or more objects have a partial gap opened to enhance the wave dissipation (Baruteau & Pa-

¹ However, a refined treatment in Deck & Batygin (2015) suggests that pairs of planets are more likely to be found near resonance following the formalism in GS14, but considering more general mass ratios.

paloizou 2013). According to Podlewska-Gaca et al. (2012), the resulting migration direction of planets may be reversed by this effect.

With the dissipative actions (e.g. density wave emission, tides) the multi-body systems may be locked into MMRs, for which the period ratios are close to ratios of integers. Notice that the analytical treatment presented in this section draws heavily from the formalism in Goldreich & Tremaine (1979) (hereafter GT79), Goldreich & Tremaine (1980) (hereafter GT80), Ward (1988) (hereafter W88). The detailed derivation of some of the formulas from GT79, GT80 and W88 are not repeated in this section, but instead cited with the corresponding equation numbers therein. As a sample problem we consider an object ‘‘A’’ moving on a *fixed* outer circular orbit and an object ‘‘B’’ moving along an inner eccentric orbit. The system is assumed to be locked in a $m : m - 1$ resonance such that

$$m\Omega_A = m\Omega_B - \kappa_B, \quad (1)$$

where Ω is the angular frequency and κ is the epicyclic frequency.

The individual gravitational field for object A or B can be Fourier-decomposed as ($s = A, B$)

$$\begin{aligned} \varphi_s(r, \phi, t) &= \sum_{\ell_s=-\infty}^{\infty} \sum_{m_s=0}^{\infty} \varphi_{s, \ell_s, m_s} \cos\{m_s\phi - [m_s\Omega_s + (\ell_s - m_s)\kappa_s]t\} \\ &= \sum_{\ell_s=-\infty}^{\infty} \sum_{m_s=0}^{\infty} \varphi_{s, \ell_s, m_s} \cos\{m_s\phi - [\ell_s\lambda_s - (\ell_s - m_s)\varpi_s]\} \end{aligned} \quad (2)$$

where we have used $\Omega_s = \dot{\lambda}_s$ and $\varpi_s = \Omega_s - \kappa_s$ (GT80). The pattern frequency of the ℓ_s, m_s component is

$$\Omega_{\ell_s, m_s} = \Omega_s + \frac{\ell_s - m_s}{m_s} \kappa_s. \quad (3)$$

The coefficients φ_{s, ℓ_s, m_s} as a function of the orbit parameters may be found in GT80. In the small eccentricity limit it is proportional to $e^{|\ell_s - m_s|}$. Therefore up to the linear order in the eccentricity only the $|\ell_s - m_s| \leq 1$ terms are relevant. Higher multiples matter if we go beyond the leading order effects. As object A is moving on a circular orbit, only $\ell_s = m_s$ term is nonzero for the expansion of its gravitational potential. The second line of Eq. (2) is more general than the first line as it does not assume the time dependent phase to be zero at $t = 0$.

The gravitational field of the object A or B resonantly excites density waves in the disc through the Lindblad and corotation resonances, transferring part of the object’s angular momentum to the disc. In particular, the inner and outer Lindblad resonances are located at

$$m(\Omega - \Omega_{\ell_s, m_s}) = \pm\kappa, \quad m > 0, \quad (4)$$

where m specifies the particular Lindblad resonance between the planets, Ω, κ are orbital and epicyclic frequencies of the fluid, which are slightly different from orbital frequencies of the embedded compact objects. Notice that the location of the inner $m : m - 1$ Lindblad resonance of object A should be close to the radius of object B, i.e.,

$$m(\Omega - \Omega_{m, m}) = m(\Omega - \Omega_A) = \kappa. \quad (5)$$

For the corotation resonance the condition is

$$\Omega = \Omega_{\ell, m}. \quad (6)$$

The density waves produced by object A, B can be decomposed into various harmonics with different azimuthal number and frequencies. Denoting φ_s^D ($s = A, B$) as the gravitational potential perturbation generated by density wave perturbations (e.g. see Eq. (16) in GT79), the non-vanishing interference term produced by the harmonics appears when the system is locked in a resonance. The relevant harmonics are given by (set the $m_A = m, \ell_A = m_A$ harmonics for φ_A and $m_B = m, \ell_B = m_B - 1$ harmonics for φ_B in Eq. (2).)

$$\begin{aligned} \varphi_A^D(r) e^{im\phi - i\omega t} &= \Phi_A e^{i \int_A^r ds k(s)} e^{im\phi - i\omega t}, \\ \varphi_B^D(r) e^{im\phi - i\omega t} &= \Phi_B e^{i \int_B^r ds k(s)} e^{im\phi - i\omega t} e^{iQ_0} \end{aligned} \quad (7)$$

with $\Phi_{A, B}$ being the amplitudes, Q_0 being a constant related to the initial phase of object B’s motion relative to object A, k being the wave number, $\omega = m\Omega_A = m\Omega_B - \kappa_B$ and the integration bottom limit can be set as the location of the Lindblad resonance. Notice that other pairs of harmonics (e.g. the $\ell_B = m_B$ harmonic term here) that do not have the same azimuthal number and frequency can not produce a nonzero angular momentum flux through interference, after performing the angular and temporal average. On the other hand, according to the discussion in GT79 (Eq. (30) therein), the angular momentum flux carried by a density wave is

$$\mathcal{F}_J = -\text{sgn}(k) \frac{mr\Phi^2}{4G} \left(1 - \frac{c^2|k|}{\pi G\sigma}\right) \quad (8)$$

where σ is the surface density, r is the radius of wave evaluation, $c^2 = dP/d\sigma$ is the square of the sound speed and Φ is the amplitude of the total φ^D . Within the thin-disc approximation it can be shown that \mathcal{F}_J is independent of r . In GT79 it is also shown that this angular momentum flux is equal to the migration torque (apart from the opposite sign) that backreacts on the object generating the density wave, which is expected from conservation of the total angular momentum.

With the superposition of density waves from object A and B, the total angular flux at a given radius receives beating terms that are proportional to the amplitudes of both waves. In particular, the beating between the harmonic components described by Eq. (7) leads to a nonzero (average-in-time) cross term

$$\mathcal{F}_{J\times} = -\text{sgn}(k) \frac{mr}{2G} \left(1 - \frac{c^2|k|}{\pi G\sigma}\right) \text{Re}(\Phi_A \Phi_B e^{i(Q_0 + C_{AB})}). \quad (9)$$

where $C_{AB} = \int_A^B ds k(s)$ is the additional phase factor coming from the wave propagation between two Lindblad resonances. This additional angular flux should correspond to additional migration torque acting on the objects, but the angular momentum conservation alone cannot determine the fraction of torque exerted on each object. It requires specific analysis for the value of the torque on each massive object. In addition, in light of the Eq. (2) it is obvious to see that the phase constant Q_0 should include the resonant angle $m\lambda_A - (m - 1)\lambda_B - \varpi_B$, where λ and ϖ are the mean longitude and longitude of pericenter respectively. Because of the dependence on the resonant angle, this additional torque (similar to the gravitational interactions) will introduce qualitatively different modification for the dynamics of the MMR, as compared to the type-I migration torques.

We shall explicit show that the nonzero flux cross term indeed gives rise to an additional torque between one planet and the density wave generated by the other planet. This torque generally averages to zero in time if the planet pair is not locked in resonance, but becomes nonzero and resonant-angle-dependent if the pair is in resonance. In Sec. 2.1 we show that for the MMR considered here, the dominant wave-planet coupling happens around the inner Lindblad resonance of planet A, which is close to the orbit of planet B as well. This observation is further verified by the numerical simulation in Sec. 3. In Sec. 2.2 we discuss the impact of this additional torque in the orbital evolution, i.e., how does it change the orbital frequency and eccentricity.

2.1 Computing the torque

For the particular Lindblad resonance shown in Eq. (5), the relevant terms in the summation of gravitational harmonics in Eq. (2) should have $m_A = \ell_A = m, m_B = m, \ell_B = m - 1$. The corresponding $\varphi_{A,B}$ have the temporal and azimuthal dependence to allow a nonzero interference torque.

The density waves produced by the external gravitational potential φ_s ($\varphi_{A,m,m}e^{im\phi-i\omega t}$ and $\varphi_{B,m-1,m}e^{im\phi-i\omega t}$) may be characterized by their associated density perturbation $\sigma_s(r)e^{im\phi-i\omega t}$ ($\omega := m\Omega_A = m\Omega_B - \kappa_B$), velocity perturbation ($u_s\hat{e}_r + v_s\hat{e}_\phi$) $e^{im\phi-i\omega t}$ and the gravitational perturbation $\varphi_s^D(r)e^{im\phi-i\omega t}$ (e.g., see GT79 for the wave equations governing these variables). In the spirit of Eq. (A7) of GT79, the torque of the external potentials $\phi_A = \varphi_{A,m,m}, \phi_B = \varphi_{B,m-1,m}$ acting on the disc is

$$T = -m\pi \int_0^\infty dr r [\phi_A(r) + \phi_B(r)] \text{Im}[\sigma_A(r) + \sigma_B(r)]. \quad (10)$$

As a result, the backreaction of the density wave produced by object A on object B should be

$$\begin{aligned} T_B &= m\pi \int_0^\infty dr r \phi_B(r) \text{Im}\sigma_A(r) \\ &= -\pi m \text{Im} \left\{ \int_0^\infty dr \left[\frac{m\phi_B\sigma v_A}{m\Omega - \omega} + ir\sigma u_A \frac{d}{dr} \left(\frac{\phi_B}{m\Omega - \omega} \right) \right] \right\} \end{aligned} \quad (11)$$

where the second line is similar to Eq. (A8) of GT79.

2.1.1 Lindblad resonances

Near a Lindblad resonance we may use a different radial coordinate $x := -1 + r/r_L$ with r_L being the radius of the Lindblad resonance. It can be obtained by requiring that (see Eq. (4))

$$D = \kappa(r)^2 - [m\Omega(r) - \omega]^2 \quad (12)$$

equals to zero at $r = r_L$. In this near zone of the Lindblad resonance, by solving the relevant wave equations the velocity perturbations can be obtained as (Appendix in GT79):

$$u_A = -\frac{\kappa}{r_L|D|} \Psi_{A,\ell,m} \int_0^\infty dt \exp \left[i \left(tx - \frac{\alpha t^2}{2\beta} + \frac{t^3}{3\beta} \right) \right] \quad (13)$$

and

$$v_A = i \text{sgn}(D) \frac{2\Omega}{\kappa} u_A \quad (14)$$

where \mathcal{D} is defined as $[rdD/dr]_{r_L}$, α is $(2\pi G\sigma r/c^2)_{r_L} \text{sgn}(k)$, β is $(r/c)_{r_L}^2 \mathcal{D}$ and $\Psi_{s,\ell,m}$ is the source term in the wave equation:

$$\Psi_{s,\ell,m} = \left(r \frac{d\varphi_{s,\ell,m}}{dr} + \frac{2m\Omega}{m\Omega - \omega} \varphi_{s,\ell,m} \right). \quad (15)$$

Here we have selected out the relevant harmonics with azimuthal number m and frequency ω . Near the MMR, although the frequency of relevant density waves generated by object A and B are both ω , the wave variables may differ by a phase offset $Q = m\lambda_A - (m-1)\lambda_B - \varpi_B$. If we use object B as the phase reference, there is an additional factor of e^{-iQ} multiplying the right hand side of Eq. (13). In addition, near the Lindblad resonance Eq.(11) can be further written as

$$T_B = -\frac{\pi m\sigma r_L}{\kappa} \text{sgn}(\mathcal{D}) \int_{-\infty}^\infty dx \Psi_{B,\ell,m} \text{Re}(u_A) f(x) \quad (16)$$

where the window function $f(x)$ is chosen such that $f = 1$ near the resonance location and $f(x) \rightarrow 0$ for $|x| \rightarrow \infty$ to eliminate oscillatory contributions far away.

Let us consider the inner Lindblad resonance of object A, near which $\Psi_{B,\ell,m}$ may be written as (Eq. 52 in W88) after taking into account the vertical average of the disc (so that the divergence is removed)

$$\begin{aligned} \Psi_{B,m-1,m} &= -e_B \frac{GmM_B}{a_B\sqrt{\pi}} \left(\frac{a_B\Omega}{c} \right) [\mathcal{F}_2(0, \xi) - 4\mathcal{F}_0(0, \xi)] \\ &+ \frac{4}{\pi} \frac{GM_B}{h\sqrt{\pi}} \sin f_c = \Psi_d + \Psi_c \sin f_c \end{aligned} \quad (17)$$

where M_B is the mass of object B, e_B is its orbital eccentricity, a_B is the semi-major axis, h is the disc height and ξ is defined as $\xi = mc/r\Omega$. Notice that for thin discs $c \sim \Omega h = \Omega r(h/r)$ so that $\xi \ll 1$ for low order m . Here f_c is related to r as

$$\frac{r}{a_B} - 1 = \gamma_0 - 1 = -e_B \gamma_0 \cos f_c \quad (18)$$

The contribution from the Ψ_c term becomes nonzero if $|1 - \gamma_0| < e_B \gamma_0$, i.e., r lies between aphelion and perihelion. The definitions of \mathcal{F} functions are expressed as integrals of modified Bessel functions (Eq. (26) of W88):

$$\begin{aligned} \mathcal{F}_0(\alpha_0, \xi) &= \pi^{-1} \int_{-\infty}^\infty e^{-(t/\xi)^2} K_0(\sqrt{\alpha_0^2 + t^2}) dt, \\ \mathcal{F}_2(\alpha_0, \xi) &= \pi^{-1} \int_{-\infty}^\infty e^{-(t/\xi)^2} \left\{ \frac{K_1(\sqrt{\alpha_0^2 + t^2})}{\sqrt{\alpha_0^2 + t^2}} - \frac{\alpha_0^2 K_2(\sqrt{\alpha_0^2 + t^2})}{\alpha_0^2 + t^2} \right\} dt. \end{aligned} \quad (19)$$

In the limit that $\xi \ll 1$, we have

$$\mathcal{F}_2(0, \xi) \approx \frac{2}{\sqrt{\pi}} \frac{1}{\xi}. \quad (20)$$

With $\Psi_{B,m-1,m}$ and u_A the torque operating on object B can be evaluated following Eq. (16). The torque T_B can be explicitly written as

$$\begin{aligned} T_{B,\text{in}} &= \frac{m\pi\sigma}{D} \Psi_{A,m,m} \int_{-\infty}^\infty dx f(x) (\Psi_d + \Psi_c \sin f_c) \\ &\times \text{Re} \left\{ \int_0^\infty dt \exp \left[i \left(tx - \frac{\alpha t^2}{2\beta} + \frac{t^3}{3\beta} - iQ \right) \right] \right\} \end{aligned} \quad (21)$$

Notice that the Ψ_d term has no explicit x dependence, so

it can be moved outside of the integral. By using the relation that (GT79, Appendix (a))

$$\begin{aligned} & \int_{-\infty}^{\infty} dx \int_0^{\infty} dt f(x) \exp \left[i \left(tx - \frac{\alpha t^2}{2\beta} + \frac{t^3}{3\beta} \right) \right] \\ & \approx 2\pi \int_0^{\infty} dt \delta(t) \exp \left[i \left(-\frac{\alpha t^2}{2\beta} + \frac{t^3}{3\beta} \right) \right] = \pi, \end{aligned} \quad (22)$$

we can identify the part of torque within T_B that is associated with Ψ_d :

$$T_{Bd} = \frac{\pi^2 m \sigma \Psi_{A,m,m} \Psi_d}{\mathcal{D}} \cos Q. \quad (23)$$

On the other hand, according to Eq. (17), the Ψ_c term in the integral of Eq. (21) has explicit dependence on x , which only makes nonzero contribution for the radius inside the orbital range $r \in [a_B(1 - e_B), a_B(1 + e_B)]$. This part of the integral is equal to ($dx = e_B \sin f_c df_c$)

$$\begin{aligned} T_{Bc} &= \frac{m\pi\sigma}{\mathcal{D}} \Psi_{A,m,m} \Psi_c \int_{-\infty}^{\infty} dx f(x) \sin f_c \Theta[e_B a_B - |r - a_B|] \\ & \quad \times \operatorname{Re} \left\{ \int_0^{\infty} dt \exp \left[i \left(tx - \frac{\alpha t^2}{2\beta} + \frac{t^3}{3\beta} - iQ \right) \right] \right\} \\ & \approx \frac{m\pi\sigma}{\mathcal{D}} \Psi_{A,m,m} \Psi_c \int_0^{\pi} e_B \sin^2 f_c f(x_0) df_c \\ & \quad \times \operatorname{Re} \left\{ \int_0^{\infty} dt \exp \left[i \left(tx_0 - \frac{\alpha t^2}{2\beta} + \frac{t^3}{3\beta} - iQ \right) \right] \right\} \\ & = \frac{m\pi^2 e_B \sigma}{2\mathcal{D}} \Psi_{A,m,m} \Psi_c \operatorname{Re} \left[W(\alpha, \beta) e^{iQ} \right] \end{aligned} \quad (24)$$

where $x_0 = a_B/r_L - 1 \sim \mathcal{O}(h^2/a_B^2)$ so that $f(x_0) \approx 1$ ², and we have defined a function $W(\alpha, \beta) := \int_0^{\infty} dt \exp \left[i \left(-\frac{\alpha t^2}{2\beta} + \frac{t^3}{3\beta} \right) \right]$ for the integral in the last line. Notice that the integral in t becomes highly oscillatory when $t > \operatorname{Min}[\beta^{1/3}, \sqrt{\beta/\alpha}]$, with $\alpha \sim r/(hQ_{\text{gas}})$, $\beta \sim \mathcal{O}(r^2/h^2)$ (Q_{gas} is the Toomre parameter). We expect both $\beta^{1/3}x_0 \ll 1$ and $\sqrt{\beta/\alpha}x_0 \ll 1$, so that the tx_0 term in the integral may be removed. The resulting T_B (by including both the T_{Bd} and T_{Bc} components) is

$$T_{B,\text{in}} = \frac{\pi^2 m \sigma \Psi_{A,m,m}}{\mathcal{D}} \left\{ \Psi_d \cos Q + \frac{e_B}{2} \Psi_c \operatorname{Re} \left[W(\alpha, \beta) e^{-iQ} \right] \right\}. \quad (25)$$

In general the two terms within the bracket together give rise to a sinusoidal term in the resonant angle Q . If we adopt the same approximation that the Toomre parameter $Q_{\text{gas}} \sim \mathcal{O}(1)$ as the analysis in (GT79), we expect $\beta^{1/3} \gg \sqrt{\beta/\alpha}$ and $W(\alpha, \beta) \approx \sqrt{\pi\beta/2\alpha} e^{-i\pi/4}$. In this limit the inner Lindblad torque becomes

$$T_{B,\text{in}} = \frac{\pi^2 m \sigma \Psi_{A,m,m}}{\mathcal{D}} \left[\Psi_d \cos Q + \frac{e_B}{2} \sqrt{\pi\beta/2\alpha} \Psi_c \cos(Q + \pi/4) \right] \quad (26)$$

On the other hand, in the limit that the disc self-gravity is negligible, we expect that $\beta^{1/3} \ll \sqrt{\beta/\alpha}$. In this limit we have

$$W(\alpha, \beta) \approx \left\{ \frac{i\Gamma(1/3)}{2 \times 3^{2/3}} + \frac{2\pi}{2 \times 3^{2/3}\Gamma[2/3]} \right\} \beta^{1/3}. \quad (27)$$

² A useful discussion regarding the difference between the fluid motion and the motion of the massive object can be found in Sec. V of Kocsis et al. (2011)

Plugging this expression into Eq. (25) we can obtain the corresponding torque expression

$$T_{B,\text{in}} \approx \frac{\pi^2 m \sigma \Psi_{A,m,m}}{\mathcal{D}} \left[\Psi_d \cos Q + 0.64 e_B \beta^{1/3} \Psi_c \cos(Q - 0.52) \right]. \quad (28)$$

For the outer Lindblad resonance of object A, $\Psi_{B,m-1,m}$ is approximately constant in the relevant resonance range, so that

$$T_{B,\text{out}} = \frac{\pi^2 m \sigma \Psi_{A,m,m} \Psi_{B,m-1,m}}{\mathcal{D}} \cos Q. \quad (29)$$

The expression is regular within the thin disc approximation so that the vertical average is not needed. Its value is given by

$$\Psi_{B,m-1,m} = -e_B \frac{GM_B}{2a_B} \left[\gamma^2 \frac{d^2 b_{1/2}^m}{d\gamma^2} - 4m\gamma \frac{db_{1/2}^m}{d\gamma} + 4m^2 b_{1/2}^m \right] \quad (30)$$

where $b_{1/2}^m(\gamma)$ are the Laplace coefficients

$$b_{1/2}^m(\gamma) \equiv \frac{2}{\pi} \int_0^{\pi} \frac{\cos m\phi d\phi}{(1 - 2\gamma \cos \phi + \gamma^2)^{1/2}} \quad (31)$$

and the above expression should be evaluated at $\gamma_0 = [(m+1)/(m-1)]^{2/3}$ in the case of a Keplerian disc. As we compare $\Psi_{B,m-1,m}$ evaluated at the inner and outer Lindblad resonance of object B, we find that $\Psi_{B,m-1,m}$ of the inner Lindblad (e.g. Eq. (17)) is larger than the one for outer resonance by a factor $\sim 1/\xi$. So the contribution from outer Lindblad resonance can be neglected for thin discs.

In summary, the density wave generated by planet A backreacts on planet B mainly in the neighborhood of the inner Lindblad resonance of planet A, which is also close to the orbit of planet B. The backreaction torque is given by Eq. (16) or Eq. (25), with the latter being derived in the vertical average approximation of the disc. Notice that when the planet pair is off resonance, there is still instantaneous torque from the wave-planet interaction. However, they generally average to zero in time as the frequency of the wave $m\Omega_A$ mismatches with the relevant harmonic frequency of the planet potential $m\Omega_B - \kappa_B$.

2.1.2 Corotation resonance

For a single object s , the torque due to corotation resonance is

$$T_{s,\text{co}} = -\frac{m\pi^2}{2} \left[\left(\frac{d\Omega}{dr} \right)^{-1} \frac{d}{dr} \left(\frac{\sigma}{B_0} \right) (\varphi_{s,\ell,m})^2 \right] \quad (32)$$

with $B_0 := \Omega + r/2d\Omega/dr$. In analogy with the case of Lindblad resonances, the interaction between density wave generated by object A and object B produces a corotation torque:

$$T_{B,\text{co}} = -\frac{m\pi^2}{2} \left[\left(\frac{d\Omega}{dr} \right)^{-1} \frac{d}{dr} \left(\frac{\sigma}{B_0} \right) \varphi_{A,m,m} \varphi_{B,m-1,m} \cos Q \right]_{r_C} \quad (33)$$

evaluated at the location of corotation resonance r_C . Notice that $\varphi_{A,m,m}$ here needs to be averaged over the vertical scale of the disc, which gives rise to (W88)

$$\langle \varphi_{A,m,m} \rangle = -\frac{2GM_A \mathcal{F}_0(0, \xi)}{r\sqrt{\pi}} \xi^{-1}. \quad (34)$$

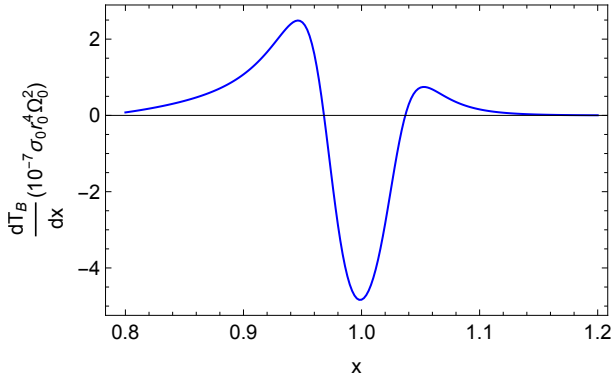


Figure 1. Torque density assuming a pair of planets trapped in a 2 : 1 resonance, with the resonance angle Q being zero and the same binary configuration used as the $e_B = 0.1$ setup in Sec. 3.

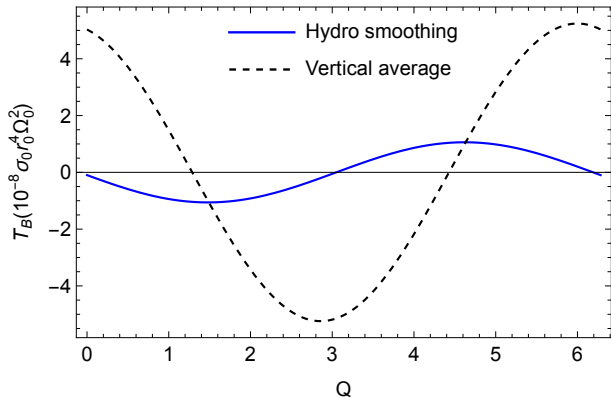


Figure 2. Comparison of the torque as a function of Q for two different smoothing schemes. The orbital configuration is the same as the $e_B = 0.1$ setup in Sec. 3.

Since the factor $\mathcal{F}_0(0, \xi) \propto \xi$ for small ξ , it means that $\langle \varphi_{A,m,m} \rangle$ has no explicit ξ dependence. On the other hand, we have

$$\varphi_{B,m-1,m} = -e_B \frac{GM_B}{2a_B} \left[\gamma \frac{db_{1/2}^m}{d\gamma} + (1-2m)b_{1/2}^m \right]. \quad (35)$$

The resulting $T_{B,\text{co}}$ is approximately $\mathcal{O}(\xi^2) \sim \mathcal{O}(h^2/r^2)$ times smaller than $T_{B,\text{in}}$, so we shall neglect this piece in the rest of the discussions.

2.1.3 Alternative smoothing scheme

In previous sections we have discussed a vertical averaging scheme introduced in W88 to regularize the torque generated around the co-orbital regime. In numerical simulation an alternative smoothing scheme is often implemented by modifying the gravitational potential produced by planets, i.e.

$$\Phi_s = -\frac{G\mu_s M}{(|\mathbf{r}_{p,s} - \mathbf{r}|^2 + \epsilon^2)^{1/2}} + \mu_s \Omega_{p,s}^2 \mathbf{r}_{p,s} \cdot \mathbf{r}, \quad (36)$$

where $s = A, B$ for each planet, the first term is the direct potential from the planet, and the second term is the indirect potential arising from the choice of our coordinate system. The smoothing parameter ϵ prevents the numerical divergence of the potential in the co-orbital regime.

With the modified potential one can compute $\Psi_{s,\ell,m}$ according to Eq. (15) and the Lindblad torque according to Eq. (16). Notice that Eq. (16) represents the total torque across the resonance, where its integrand represents the torque density. In Fig. 1 we show the torque for a 2 : 1 resonance case, with $\epsilon = 0.6h$ and other parameters consistent with the numerical simulation discussed in Sec. 3. We indeed find torque density centred around the location of the inner Lindblad resonance.

In Fig. 2 we compare the interference torques computed using two different smoothing schemes. The smoothing scheme consistent with hydrodynamical simulations is based on Eq. (16) and Eq. (15), whereas the torque associated with the vertical average scheme discussed in Sec. 2.1.1 uses Eq. (25). The two predictions are different, which must come from different regularization methods used for contribution of disc materials in the corotation regime. Therefore an accurate quantification of the interference torque should include a three dimensional calculation.

2.2 Change rate of orbital quantities

The additional torque due to interfering density waves affects the orbital motion of object B. In this section we evaluate the corresponding e_B and \dot{n}_B , where n_B is the mean motion. We also assume a Keplerian disc profile to simplify the calculations, which may also serve as order-of-magnitude estimation for more general scenarios. For a Keplerian disc we expect

$$\mathcal{D} = 3(m-1)\Omega_B^2. \quad (37)$$

and

$$\frac{\beta}{\alpha} = \frac{3(m-1)}{M} 2\pi\sigma a_B^2. \quad (38)$$

To evaluate the Lindblad torque in Eq. (25) $\Psi_{A,m,m}$ is also required:

$$\Psi_{A,m,m} = -\frac{GM_A}{r_A} \left[\gamma \frac{db_{1/2}^m}{d\gamma} + 2mb_{1/2}^m \right]_{\gamma} \quad (39)$$

where γ should be set as $\gamma = (1-1/m)^{2/3}$. For a particular $m-1 : m$ MMR between object B and A, only the density waves with the same m are relevant for obtaining the ‘‘resonant torque’’. Let us consider the case with $m = 2$ which will be further discussed in Sec. 4:

$$\Psi_{A,2,2} = -2.4 \frac{GM_A}{r_A}. \quad (40)$$

For object B’s orbit, the change rate of eccentricity due to the additional torque is (W88)

$$\frac{1}{e_B} \frac{de_B}{dt} = \left[\Omega_{m-1,m} - \Omega_B - 2e_B^2 \Omega_B \left(1 + \frac{d \log \kappa}{d \log r} \right)_{r=a} \right] \times \frac{T_{B,\text{in}}}{M_B e_B^2 a_B^2 \kappa^2} \quad (41)$$

where we only use the dominant contribution from $T_{B,\text{in}}$. In the case of a Keplerian disc and that $e_B \ll 1$, the e_B^2 term within the square bracket can be neglected and the \dot{e}_B simplifies to

$$\frac{de_B}{dt} = \frac{-1}{m} \frac{T_{B,\text{in}}}{M_B e_B a_B^2 \Omega_B} := -\frac{\cos(Q-Q_0)}{\tau_0} \quad (42)$$

so that the sign of \dot{e}_B depends on the relative phase Q_0 encoded in the $\cos(Q - Q_0)$ term. In order to compute n_B , we use the energy balance equation that

$$\frac{dE}{dt} = \Omega_B T_{B,\text{in}} \quad (43)$$

which naturally leads to

$$\begin{aligned} \dot{n}_B/n_B &= -3(GM)^{-2/3} n^{1/3} M_B^{-1} T_{B,\text{in}} \\ &:= -\frac{3me_B}{\cos} (Q - Q_0) \tau_0. \end{aligned} \quad (44)$$

In general τ_0 and Q_0 should be obtained and calibrated with three-dimensional hydro-simulations. In Sec. 4 we investigate the simplest scenarios with Q_0 being 0 or π (or equivalently τ_0 being either positive or negative) where the resonant dynamics shows distinctive features.

3 HYDRODYNAMICAL SIMULATIONS

3.1 Numerical Setups

In order to further demonstrate the effect of interfering density waves beyond the analytical calculations, a few hydrodynamical simulations are carried out to confirm the effect of interfering density waves on the dynamics of the MMR pair. We use the FARGO3D code (Benítez-Llambay & Masset 2016) to simulate the gravitational interaction of a pair of (or a single) planet with a 2D thin disc. The disc aspect ratio is initialized as $h/r = 0.05$ and is constant over the entire disc. As a result, we set a locally isothermal equation of state with a temperature profile of a power-law index of -1.0 . The surface density is set as $\sigma = \sigma_0 (r/r_0)^{-0.5}$ initially, where $\sigma_0 = 3 \times 10^{-5} M/r_0^2$ is the surface density at r_0 , where M is the stellar mass, r_0 is the typical length scale of the disc, which can be scaled freely to compare with observations. Such a low surface ensures that the disc self-gravity can be safely ignored in simulations. We also assume an α -prescription for the gas kinematic viscosity $\nu = \alpha_{\text{vis}} h^2 \Omega$ (Shakura & Sunyaev 1973). A moderate $\alpha_{\text{vis}} = 0.01$ is adopted to ensure that both planets do not open deep gaps in the disc.

A pair of planets is orbiting around the central star at a fixed orbit with the orbital semi-major axis $a_B = 1.0 r_0$ and $a_A = 2^{2/3} \left(\frac{1+\mu_B}{1+\mu_A} \right)^{-1/3} r_0$, where $\mu_B = 10^{-5}$ and $\mu_A = 3 \times 10^{-5}$ are the mass ratio of the inner and outer planets. This orbital configuration ensures that the two planets are in 2:1 MMR. Other planet pairs with 3:2 MMR is discussed in Sec. 3.2.3 with a_A modified accordingly. Such small mass ratios for both planets are chosen to ensure that the tidal response of the disc is in the Type I regime. Note that the theory in the Sec. 2 should also be valid even though the mass ratio of the pair does not satisfy $\mu_A \gg \mu_B$. For our fiducial case, the inner planet is fixed at an eccentricity of $e_B = 0.03$, while the outer one moves along a nearly circular orbit with $e_A = 0.001$. Both planets have a longitude of pericenter of $\varpi_A = \varpi_B = 0.0$. The dependencies of ϖ_B and e_B have also been explored. The back reaction of disc force and mutual interaction for each planet is turned off such that both planets are fixed at the prescribed orbits described above. In this way, we can evolve both planets in a controlled manner, and make better comparison with our theory. With this kind of setup, both planets have a resonance angle of $Q = 0.0$.

The gravitational potential for each planet of the pair is described as Eq. (36). We apply a gravitational softening, with length scale $\epsilon = 0.6h$, to each planet's potential.

We evolve the disc in a 2D cylindrical coordinate with a uniform radial grid of $n_r = 384$ points in a radial domain between $[0.2, 4.0]r_0$, and a uniform azimuthal grid with $n_\phi = 640$ points. A convergence test with higher resolutions $[n_r, n_\phi] = [512, 1024]$ does not show significant impact on the dynamics of the planet pair. Two wave-killing zones are applied at the both the inner and outer radial edge to remove wave reflections near both boundaries (de Val-Borro et al. 2006).

3.2 Simulations Results

3.2.1 Non-Resonant Pairs

Before we probe the existence of interfering density waves, we first run one planet pair simulations with their orbital period ratio is away from any MMR, e.g., we set $a_B = 1.0$, and $a_A = 1.7$. Under such circumstance, the resonance angle of both planets circulates about the full 2π , regardless of the value of ϖ_A and ϖ_B . The time-averaged interference torque should vanish due to the $\cos Q$ -like dependence. To verify this, we further run one single planet simulations with its orbit fixed in the same radius as the inner planet of the pair case.

We can then track the torque acting on the inner planet for both cases. The time-averaged radial profile of the torque is shown in the upper left panel of Fig. 3. We can see that the single planet can well reproduce the torque acting on the inner planet for the pair case, which means that the time-averaged torque induced by the density perturbation of the the outer planet vanishes as expected. To further confirm this, we also run another single planet simulation with its orbit being same as the outer planet of the planet pair, and a zero-mass inner passive particle is added to follow in the inner planet orbit. The torque acting on the passive inner planet, which is due to the density perturbation induced by the outer planet, can be instantaneously tracked. The time evolution and time-averaged value of the torques are shown in the lower left panel of Fig. 3. It can be clearly seen that the time-averaged interference torque due to the outer planet is consistently zero although the instantaneous torque magnitude is large. This essentially demonstrate the net zero interference torque for the non-MMR pair, as expected from the $\cos Q$ -like dependence.

Furthermore, we test the dependence on the inner planet eccentricity, as shown in the right panels of Fig. 3. Here we increase the inner planet eccentricity to $e_B = 0.1$. Similar to the low eccentricity case in the left panels, the gravitational torques from the single planet located in the inner orbit are consistent with those of the planet pair case after performing the time-averaged procedure. Note that the cumulative torque on the planet is positive. This is because the gravitational torque significantly depends on the eccentricity. For low eccentricity orbits, e.g. the $e_B = 0.03$ case, the cumulative torque is indeed negative. When the eccentricity is much higher, e.g. the $e_B = 0.1$ case, the cumulative torque becomes positive which mainly damps out the eccentricity, with the semi-major axis still *decreasing* in time.

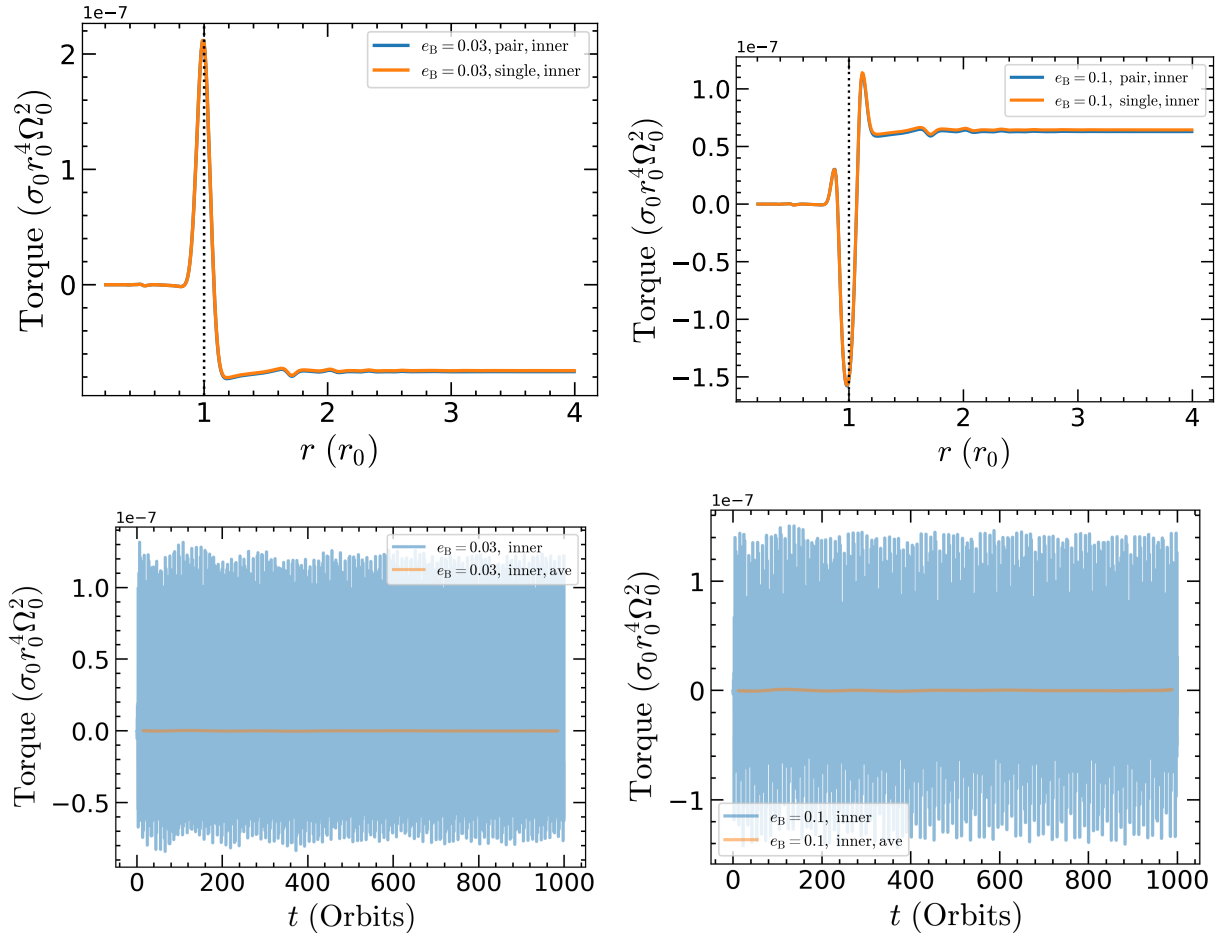


Figure 3. Upper Left: the cumulative gravitational torque on the embedded objects as a function of r for different models with the inner planet eccentricity $e_B = 0.03$. The blue line shows the torques for the inner planet based on the planet pair simulation, while the orange line shows the torque from the inner single planet case. The dotted line indicates the location of the inner planet. The cumulative torque is obtained by integrating the differential torque density over r from the inner boundary to a given r . All the torque calculations are time-averaged within 100 orbits around 1000 orbits. Lower Left: the time evolution of the interference torque on the inner planet location. The blue line shows the instantaneous torque while the orange one is the time-averaged value. We can see that the single planet simulation can well reproduce the torques in the planet pair simulations, which means no net interference torque on the inner planet averaged over time when the pair is out of MMR. Right panels: similar to the left ones except that the inner planet eccentricity is fixed at $e_B = 0.1$.

3.2.2 Planet Pairs with 2:1 MMR

Now we explore the interference term when the planet pair is fixed at the 2:1 MMR configuration and a resonance angle for the inner planet at $Q = 0.0$, as described above. We carry out two single-planet simulations with each one set at the orbital configuration of the inner or outer planet of the pair, respectively. We can then calculate the torques on the inner planets for both the single planet and planet pair simulations to probe the existence of interfering density waves. The cumulative radial profile of the torques for single and pair cases with $e_B = 0.1$ are shown in Fig. 4. There is a remarkable difference for the time-averaged torque on the inner planet between the planet pair and single planet cases. This torque difference closely matches the interference torque due to the outer planet’s perturbation, shown as the dashed line in the same plot. This time-averaged interference torque is not vanishing due to the approximately constant Q in the MMR regime.

The difference of the torque between the planet pair and

single planet cases shown in Fig. 4 can then be used to compare with the analytical theory for the additional torque associated with the interfering density wave. The torque due to the interfering density wave for the inner planet measured directly from simulation (the difference between the blue and orange lines in Fig. 4) is about $\sim -2.9 \times 10^{-8}$ (in code unit), also shown as the black line in Fig. 5 with $Q = 0.0$. The location of the torque jump is located exactly at the inner Lindblad resonance for the outer planet of the pair. In order to explore the dependence of the resonance angle Q , we further run a few simulations with different ϖ_A and ϖ_B . The results of the interference torque for different Q with $e_B = 0.1$ are shown as the black line in Fig. 5. We can see that the sinusoidal-like pattern of the interference torque with respect to Q can be reproduced from our numerical simulations, although the pattern does not exactly follow the sinusoidal dependence with a single frequency in Q . This may suggest that there are high orders of harmonics of Q in the interference torque, which are neglected in the

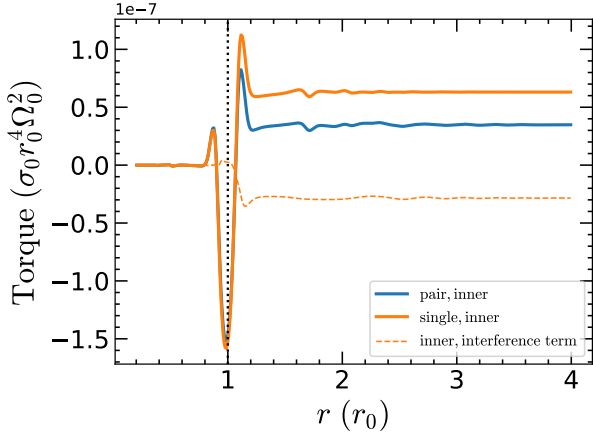


Figure 4. Similar to the upper right panel of Fig. 3 with $e_B = 0.1$, but for the case when the planet pair is in 2:1 MMR with a resonance angle of $Q = 0$. The dashed line shows the time-averaged interference torque due to the density wave generated by the outer planet acting on the inner planet. All the torques are averaged within 100 orbits around 1000 orbits. We can see that after the planet pair being captured into MMR, there exists significant torque difference for the inner object between the single planet and planet pair simulations.

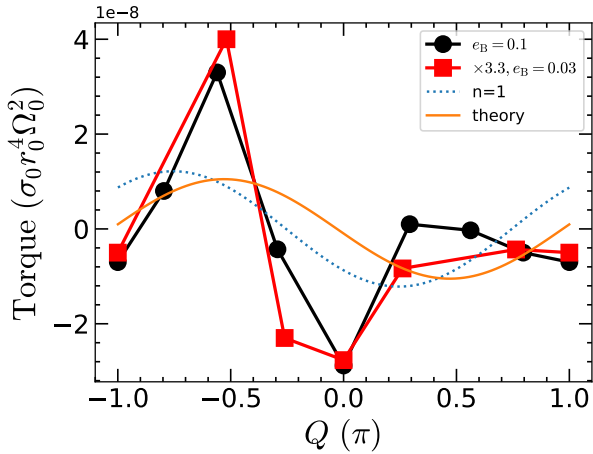


Figure 5. The interference torque as a function of the resonance angle for the inner planet. The black line shows the case where the inner planet has an eccentricity $e_B = 0.1$ while the red line corresponds to the case where $e_B = 0.03$. Considering the linear dependence of the interference torque on e_B , we scale up the red line by a factor of 3.3. We can see that this linear dependence of the interference torque on e_B is quite well. The dotted line is the projection onto the $n = 1$ component for the simulated interference torque, and the solid orange line is the theoretical prediction to compare with the dotted line.

analytical theory which only considered $|\ell - m| \leq 1$ case. To filter out the high-order harmonics, we make the projection for the simulation data onto the $n = 1$ component of $A_{Tb} \sin nQ + B_{Tb} \cos nQ$. The coefficients A_{Tb}, B_{Tb} are obtained from the integration $\frac{1}{\pi} \int_0^{2\pi} T_{B, \text{sim}}(Q) \sin Q dQ$ and $\frac{1}{\pi} \int_0^{2\pi} T_{B, \text{sim}}(Q) \cos Q dQ$ respectively. The $n = 1$ component of the interference torque from the simulation data is indicated as the blue dotted line in Fig. 5.

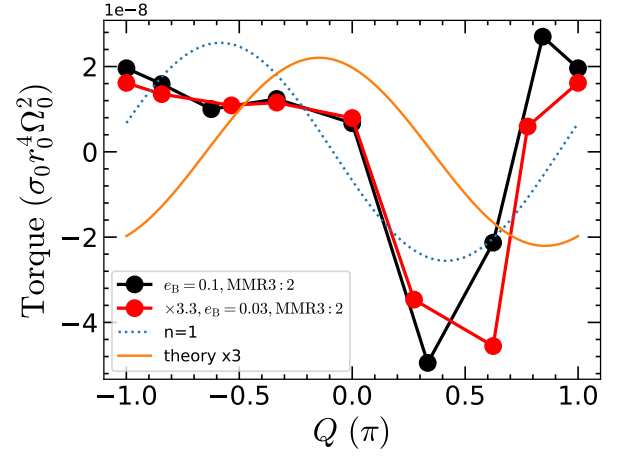


Figure 6. Similar to Fig. 5 but for 3:2 MMR. Note that the orange curve has been multiplied by a factor of 3 to match the magnitude of $n = 1$ curve from the simulation data.

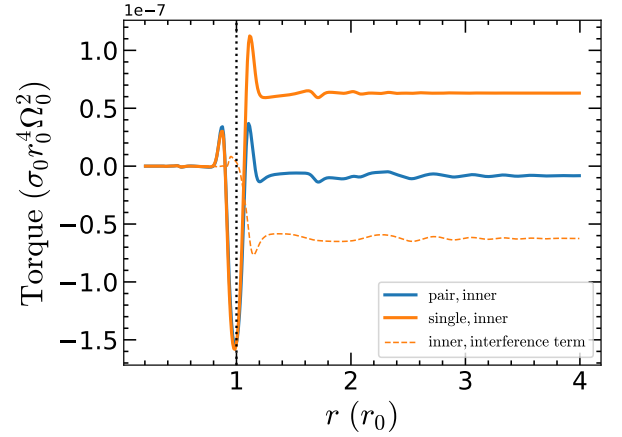


Figure 7. Similar to Fig. 4, but with the outer planet mass ratio of $\mu_A = 6 \times 10^{-5}$, which is a factor of two larger.

In the limit of the disc self-gravity is negligible, our analytical theory in Sec. 2.1.3 predicates that the additional $n = 1$ component torque from the interfering density wave can be estimated based on Eq. (16) assuming a Keplerian disc, which is shown as the orange line in Fig. 5. This is roughly consistent with that expected from our simulation results both in magnitude and phase dependence, although some discrepancy exists in the phase. There are still important differences in the assumption made in the analytical theory and the numerical simulation shown here, despite both are using the same smoothing scheme. First, the theory assumes polytropic equation of state, while the disc in our simulations is locally isothermal. Second, the theory assumes no viscosity in the disc, but a non-negligible α -viscosity is adopted in our simulations to maintain the Type I migration regime. The slightly non-Keplerian disc due to the pressure gradient will shift the resonance location from exactly 2:1 MMR location, which may impose a considerable effect on the torque.

We have confirmed from simulations that this interfering density wave is weaker for the outer planet.

3.2.3 Other Parameter Dependence

It is interesting to further explore parameter dependence of the interface torques. The first one is the linear dependence on the inner planet e_B which appeared in $\Psi_{B,l,m}$ in Equation 16. To this end, we carry out a few simulations with $e_B = 0.03$, and the results for the interface torques are shown as red dots in Fig. 5. On the one hand, as we scale the overall torque amplitude for the simulations with two different eccentricities, we find that the interference torque is approximately linear in e_B , which is consistent with the expectation from the linear theory. On the other hand, the relative contribution from high orders of harmonics seems to be weaker for the lower eccentricity case as we compare the simulations with two separate eccentricities.

Second, we also perform several simulations for planets locked in 3:2 MMR for both $e_B = 0.1$ and $e_B = 0.03$ with different Q . The results are shown in Fig. 6. The $n = 1$ component of the simulated interference torques are shown as the dotted line, and the theoretical prediction based on Eq. (16) is represented as the solid orange line. The linear dependence on e_B is quite similar to the 2:1 MMR case. However, in order to match the torque magnitude for the simulation data, the theoretical curve in Fig. 6 has been multiplied by a factor of 3. The phase offset between the theory and simulation curves is also larger than that of 2:1 MMR. This suggests that there may exist important factors that lead to such deviation, with some possible reasons discussed above.

Third, we further examine the mass ratio dependence for the interference torque, which should be proportional to the mass of the both planet (ref. to Eq. (16) or Eq. (21) for the dependence on $\Psi_{A,m,m}$ and $\Psi_{B,l,m}$). We increase the mass of the outer planet by a factor of two, and fixed the other model parameters as in Fig. 4. The results are shown in Fig. 7. We can see that the interference torque is quite similar to that of Fig. 4 except that the magnitude is also a factor of two larger, as expected.

In summary, by considering the comparison between the numerically extracted torque and analytically predicted torque, i.e., the location of the torque jump which locates at the inner Lindblad resonance, the torque amplitudes, the linear dependence on e_B , planet mass, and the sinusoidal-like pattern of the additional torque term, it is fair to state that the existence of the interference torque is evident.

4 MODIFIED RESONANT DYNAMICS

As discussed in Sec. 2, for a pair of massive objects embedded in an accretion disc and trapped within an MMR, the interfering density waves produces a backreaction torque that depends on the resonant angle Q . Such Q -dependence likely introduces qualitatively different resonant dynamics from those systems involving only gravitational interactions, or those only include constant (in the resonant angle) migration torques. We address the associated dynamical signatures in this section.

Without including the torque from interfering density waves, the equations of motion for the pair of objects considered in Sec. 2 has already been discussed in GS14, in which case the outer object A stays at a fixed circular orbit ($\dot{r}_A = 0$) and the inner object B migrates outwards. The equations of

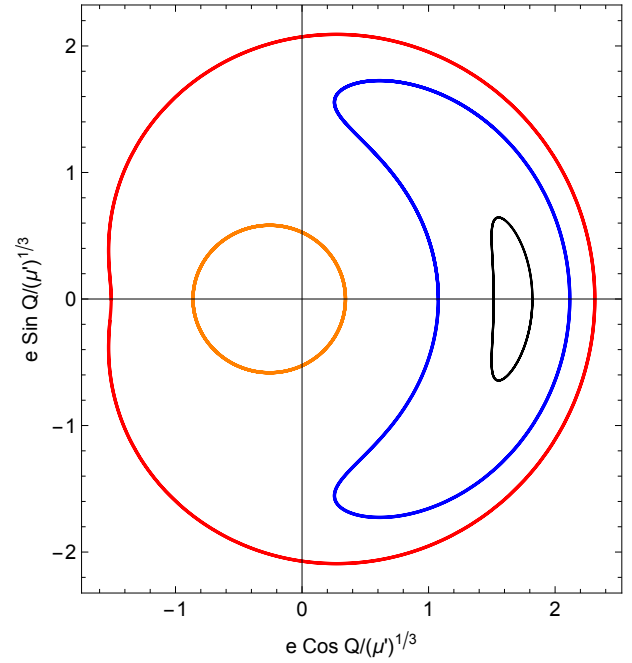


Figure 8. The phase space trajectories of a 2 : 1 resonance with $k = 2k_{\text{crit}}$.

motion including the effect of interfering density waves for $n = \dot{\lambda}_B$, e (the eccentricity of the inner planet e_B)³ are

$$\begin{aligned} \dot{n} &= 3(m-1)\beta_0\mu'en^2\sin Q - \frac{n}{\tau_n} + p\frac{e^2n}{\tau_e} - \frac{6en\cos Q}{\tau_0} \\ \dot{e} &= \beta_0\mu'n\sin Q - \frac{e}{\tau_e} - \frac{\cos Q}{\tau_0} \end{aligned} \quad (45)$$

where β_0 is approximately $0.8(m-1)$, $\mu' := M_A/M$, $\mu := M_B/M$, the p -related term may be contributed by remote first-order Lindblad resonances and corotation resonances. For illustration of principles we take the same value $p = 3$ as used in GS14. On the other hand, the change rate of mean motion and eccentricity due to single-body migration torques approximately scale as

$$\frac{1}{\tau_n} \sim \mu \frac{\sigma a^2}{M} \left(\frac{a}{h}\right)^2 n, \quad \frac{1}{\tau_e} \sim \mu \frac{\sigma a^2}{M} \left(\frac{a}{h}\right)^4 n. \quad (46)$$

The resonant dynamics can be determined by combining Eq. (45) with the definition that $Q = m\lambda_A - (m-1)\lambda_B - \varpi_B$ and the equation of motion for ϖ_B :

$$\dot{\varpi}_B = -\frac{\beta_0\mu'}{e}n\cos Q. \quad (47)$$

4.1 Without constant migration torques

Let us first consider the case with the normal migration torques turned off, i.e. removing τ_e, τ_n -related terms in Eq. (45). Although this assumption is made to present a simplified discussion on the resonant dynamics, it becomes a reasonable approximation if $\mu' \gg \mu$, although in this case n' is generally time-dependent. If the τ_0 -related term is also

³ We drop out the subscript ‘‘B’’ hereafter unless otherwise noted since we only focus on the dynamics of the inner planet.

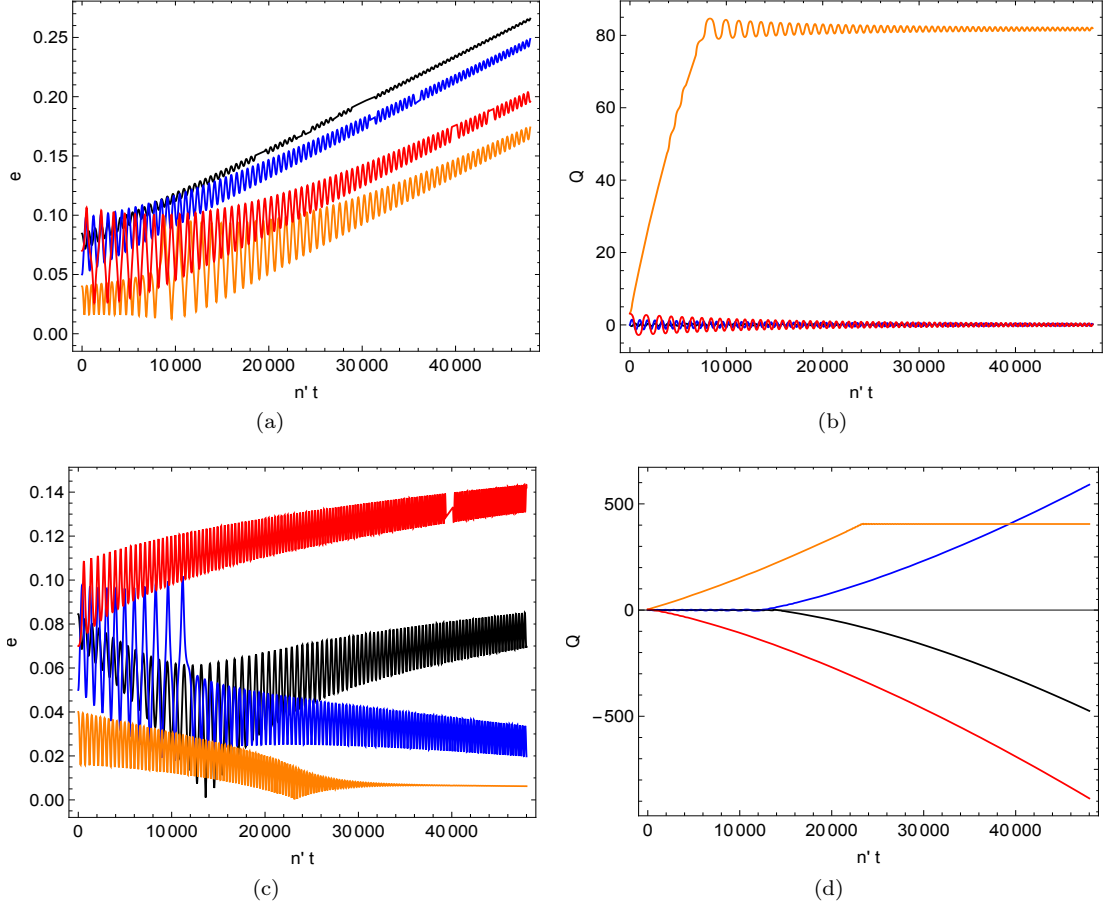


Figure 9. The evolution of the four trajectories presented in Fig. 8 with $\tau_0\beta_0\mu'n' = 20$ (top panels) and $\tau_0\beta_0\mu'n' = -20$ (bottom panels). The color scheme is chosen such that it is consistent with the phase-space trajectories in Fig. 8 as initial data.

absent, the equations of motion is compatible with the resonant Hamiltonian (GS14):

$$\mathcal{H} = ke^2 - \frac{3}{4}(m-1)^2 e^4 + 2\beta_0\mu'e \cos Q \quad (48)$$

with

$$k := \frac{3}{2}(m-1)^2 e^2 - \frac{\beta_0\mu'}{e} \cos Q + \frac{\dot{Q}}{n} \quad (49)$$

being a constant in time. The conjugate canonical variables are Q and e^2 . Defining a critical k as $k_{\text{crit}} = 3^{4/3}((m-1)\beta_0\mu')^{2/3}/2$, the phase space contains one stable fixed point for cases with $k < k_{\text{crit}}$ and two fixed points plus one unstable fixed point for $k > k_{\text{crit}}$ (Murray & Dermott 2000; Goldreich & Schlichting 2014). In Fig. 8 we show several representative phase space trajectories in terms of a set of rescaled canonical variables $\{e \cos Q/\mu'^{1/3}, e \sin Q/\mu'^{1/3}\}$. The blue and black curves are “libration” trajectories around a fixed point at $e_{\text{max}} \approx 1.96(\beta_0\mu')^{1/3}$ on the positive side of the real axis. The red curve is a large “rotation” orbit. The orange curve is a “rotation” trajectory around the other stable fixed point at $e_{\text{min}} \approx 0.093(\beta_0\mu')^{1/3}$ on the negative side of the real axis.

Now with the τ_0 term included, it contributes to another Q -dependent driving source that has 90-degree offset from the

mutual gravitational interaction. The ratio of magnitudes is

$$\begin{aligned} \frac{1}{|\tau_0\beta_0\mu'n|} &\sim 0.4 \left(\frac{\sigma a^2/M}{10^{-3}} \right) \left(\frac{a/h}{10} \right)^2 \\ &\sim \left(\frac{\alpha}{0.1} \right)^{-1} \left(\frac{\dot{M}}{0.1\dot{M}_{\text{Edd}}} \right)^{-3} \left(\frac{M}{10^5 M_\odot} \right) \left(\frac{a}{10^3 M} \right)^{5.5} \end{aligned} \quad (50)$$

which may be comparable to one depending on the properties of the disc and the location of the object, so that the resonant dynamics may be significantly affected. In the first line we have noticed that a significant fraction of protoplanetary discs in the Lupus complex observed by the Atacama Large Millimeter/Submillimeter Array has disc gas mass to star mass ratio around 10^{-3} (Ansdell et al. 2016). In the second line we have assumed a α disc profile around a supermassive black hole (Kocsis et al. 2011), with \dot{M} being the accretion rate of the central black hole and \dot{M}_{Edd} being the Eddington accretion rate.

In Fig. 9 we present the evolution in the regime that $|\mu'n\tau_0| \gg 1$, so that the force due to interfering density waves is much weaker than the gravitational interactions between the two objects. In addition, as discussed in the Sec. 3, the sign of the backreaction torque depends on the detail three-dimensional structure of the gas flow near the inner Lindblad resonance, which is not resolved in this study. As a result,

we consider two cases with $\tau_0\beta_0\mu'n' = \pm 20$ respectively. One common feature of these two scenarios is that the numerical evolution no longer preserves the area in the phase space of the canonical variables, so the evolution is no longer Hamiltonian.

In the case that $\tau_0\beta_0\mu'n' = 20$, we find various initial data all lead to an asymptotic libration state with increasing eccentricity. In fact, on the right hand side of the \dot{e} equation in Eq. (45), the time average of $\beta_0\mu'n \sin Q$ is slight larger than the time average of $\cos Q/\tau_0$, so that the libration regime drifts towards to the right. On the other hand, in the case that $\tau_0\beta_0\mu'n' = -20$, we find different kinds of final states. For the black and red trajectories, the system evolve to a rotation state around the origin with increasing eccentricity in time (similar to the red curve in Fig. 8 with increasing amplitude). The blue trajectory instead lands on another rotation state with shrinking eccentricity in time (similar to the orange curve in Fig. 8 with decreasing amplitude).

Mathematically we can approximately describe the end state of the black and red trajectory as follows. Without the τ_0 -related terms, the rotational orbits around the origin can be written as

$$\begin{aligned} n &= n_0 + \epsilon \delta n \cos Q + \mathcal{O}(\epsilon^2), \\ e &= e_0 + \epsilon \delta e \cos Q + \mathcal{O}(\epsilon^2), \\ Q &= \omega_0 t + \mathcal{O}(\epsilon) \end{aligned} \quad (51)$$

where ϵ is a book-keeping parameter and we only keep terms up to the linear order in ϵ . In addition, according to the fact that

$$\dot{Q} = mn' - (m-1)n + \frac{\beta_0\mu'}{e} \cos Q, \quad (52)$$

we can immediately identify that $\omega_0 = mn' - (m-1)n_0$. Together with Eq. (45) (with τ_0, τ_n, τ_e -related terms removed), we find that

$$\begin{aligned} \delta n &= -\frac{3(m-1)\beta_0\mu'e_0n_0^2}{\omega_0}, \\ \delta e &= -\frac{\beta_0\mu'n_0}{\omega_0}. \end{aligned} \quad (53)$$

In order to describe the secular evolution, we can use the evolution of conserved quantities k, \mathcal{H} :

$$\begin{aligned} \frac{dk}{dt} &= 3e\dot{e}\tau_0 - \frac{2n'}{n^2}\dot{n}\tau_0 = \frac{3e \cos Q}{\tau_0}, \\ \frac{d\mathcal{H}}{dt} &= e^2 \frac{dk}{dt} + \frac{de^2}{dt} \left(k - \frac{3}{2}e^2 + \beta_0\mu'/e \cos Q \right) \\ &= \frac{3e^3 \cos Q}{\tau_0} - \frac{2e \cos Q}{\tau_0} \left(k - \frac{3}{2}e^2 + \beta_0\mu'/e \cos Q \right) \\ &= -\frac{2e \cos Q}{\tau_0} (k - 3e^2) - \frac{2\beta_0\mu' \cos^2 Q}{\tau_0}. \end{aligned} \quad (54)$$

After plugging the approximate solution in Eq. (51) and Eq. (53) and performing average over oscillation cycles in the resonant phase Q , we find that (with $m=2$)

$$\langle \dot{k} \rangle = -\frac{3\mu'\beta_0n_0}{\omega_0\tau_0} \left(1 + \frac{3n_0e_0^2}{2\omega_0} \right), \quad (55)$$

which is also useful for the analysis in Sec. 5. On the other

hand, the orange curve eventually evolves to a state that

$$\begin{aligned} \beta_0\mu'n \sin Q &\approx \frac{\cos Q}{\tau_0}, \\ mn' - (m-1)n + \frac{\beta_0\mu'}{e} n \cos Q &\approx 0, \end{aligned} \quad (56)$$

i.e., $\dot{e}, \dot{Q} \approx 0$, so that the quasi-stationary values of e, Q can be determined as functions of n . Notice that here n is still time dependent according to Eq. (45) (with $1/\tau_e, 1/\tau_n$ set to be zero), so that this point drifts in time. In addition, from the second line of Eq. (56) one can find that at equilibrium the offset of period ratio $mn'/n - (m-1)$ is inversely proportional to the eccentricity, i.e., smaller eccentricity corresponds to larger offset of the period ratio (see also the related discussion in Sec. 3). This is a rather general point as long as Q is bounded.

4.2 With migration torques

With the results from Sec. 4.1 we can now discuss evolutions in the more general settings, with the migration torques turned on. In GS14 with no τ_0 -related terms in the equation of motion, it is shown that there are three parameter regimes of interest. The system is trapped in resonance with fixed Q and e for

$$\mu' > \frac{(m-1)}{\sqrt{3}m^{3/2}\beta_0} \left(\frac{\tau_e}{\tau_n} \right)^{3/2} \quad (57)$$

and for

$$\mu' < \frac{(m-1)^2}{8\sqrt{3}m^{3/2}\beta_0} \left(\frac{\tau_e}{\tau_n} \right)^{3/2} \quad (58)$$

the system is trapped in resonance in finite duration $\sim \tau_e$. When the resonance locking breaks down the system evolves with monotonically changing period ratios and decreasing eccentricities. Between these two limits the system asymptotes a state with finite libration amplitude. Notice that the actual transition between resonance locking and rotational orbits in the phase space may significantly differ from the analytical criteria in Eq. (58) for small μ' and/or τ_n , because the adiabatic approximation used to derive the analytical formulas may break down (GS14).

In Fig. 10 we present the evolution of a pair of planets according to Eq. (45) but with the interfering density waves terms neglected. These figures essentially show the same qualitative features as Fig. 5 in GS14. In the top row where $\tau_e = \tau_n/50$, the system exits the resonance within $\sim \tau_e$ timescale and follows with monotonic period ratios afterwards. Notice that although the period ratio is monotonically changing in this regime, we find that the resonant angle Q is bounded (also see related discussion in Sec. 3). This is because the contribution from $mn' - (m-1)n$ is canceled with $\dot{\varpi}_B$. It is also particularly interesting because if Q stays bounded, the interfering density wave effect stays in operation even if the period ratio is out of resonance-locking, as discussed in Sec. 3. In the middle row with $\tau_e = \tau_n/100$, the system undergoes finite amplitude libration in the phase spacetime, so that both the eccentricity and period ratio oscillates around a fixed value. In the bottom row with $\tau_e = \tau_n/200$, the system asymptotes to a state with a fixed eccentricity ~ 0.03 and a period ratio offset ~ 0.005 .

With the τ_0 terms included, the evolution may be modified

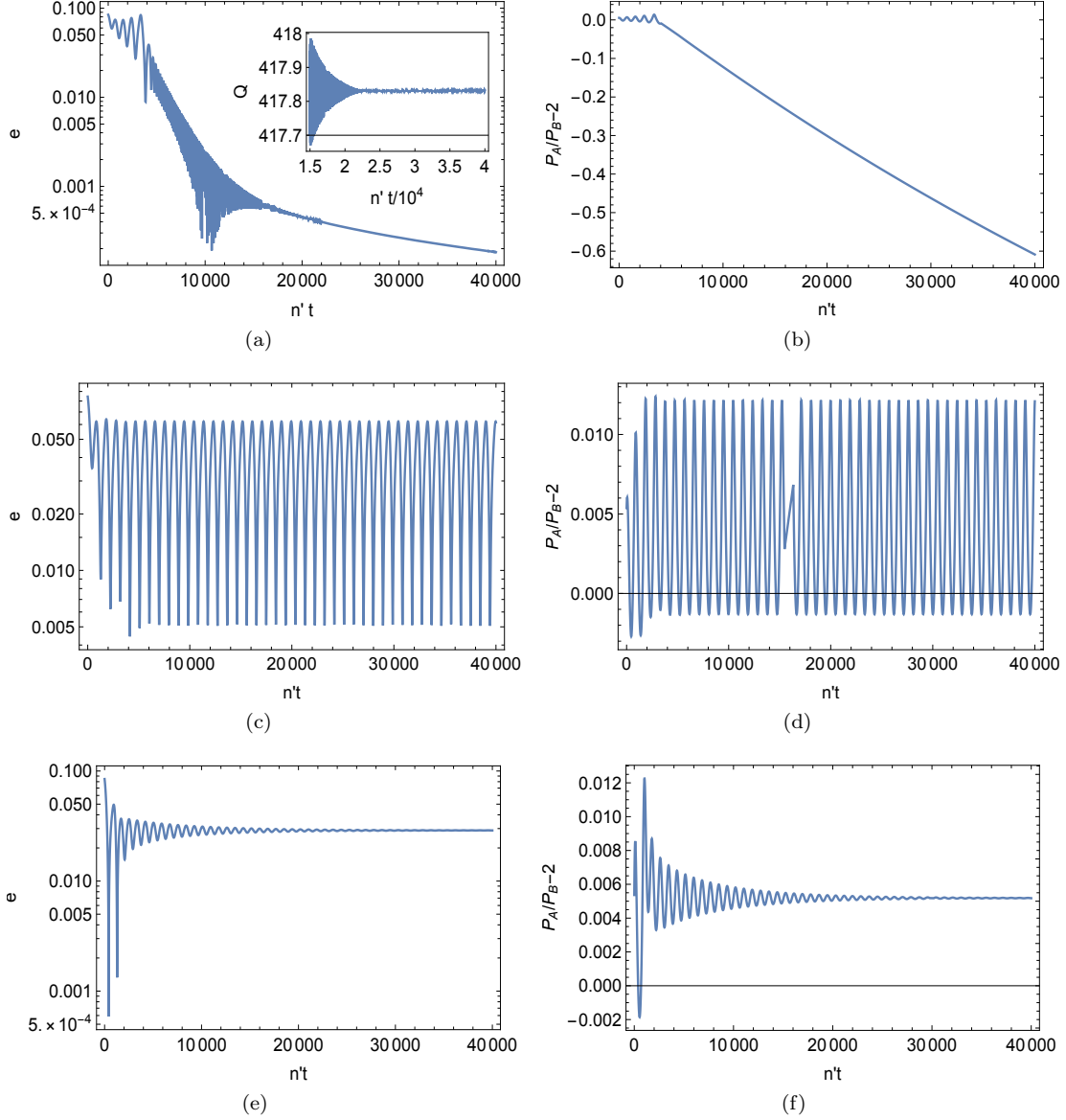


Figure 10. The evolution of eccentricities and periods with $\tau_e = \tau_n/50$ (top row), $\tau_e = \tau_n/100$ (middle row) and $\tau_e = \tau_n/200$ (bottom row) respectively, according to Eq. (45) but with τ_0 terms turned off. The scaled mass of object A is assumed to be $\mu' = 10^{-4}$ and τ_n is set to be $n'\tau_n = 10^5$. The inset of panel (a) shows the evolution of the resonant angle Q , which is bounded at late times.

significantly. In Fig. 11 we present the case with the same parameters as in Fig. 10 but with $\tau_0 = \pm\tau_n/10$. For the positive τ_0 cases, the system preferably lends on an asymptotic state with constant resonant angle and eccentricity (not shown in the plot). The period ratios are also asymptotically constant with $\leq 0.3\%$ difference from 2. On the other hand, for the negative τ_0 case, the system no longer exhibits finite amplitude libration as shown in panel (c,d) of Fig. 10, but instead loses the resonance locking without keeping bound Q . The period ratios are monotonically decreasing for the cases with $\tau_e = \tau_n/50$ and $\tau_e = \tau_n/100$, but oscillating around a fixed value for $\tau_e = \tau_n/200$. In the latter case the phase-space trajectory is qualitatively similar to the red trajectory in Fig. 8. Based on this particular system setup, it seems negative τ_0 more likely drives the system far away from resonant period

ratios, which is a phenomenon to be understood from the *Kepler* observations (Deck & Batygin 2015).

In order to understand the “end state” of the system with the influence of τ_0 terms for a larger range of parameters, we perform a series of numerical evolutions using Eq. (45) but with different τ_e and τ_0 . For each set of evolution we extract the period ratio at the end of the simulation, with $t_{\text{end}}n' = 5 \times 10^4$. In the top left panel of Fig. 12, such an evolution is shown for $1/\tau_0 = 0$. We find that roughly between $\tau_n/\tau_e \sim 180$ and $\tau_n/\tau_e \sim 70$ the “end-state” period ratios show variations at the fixed end-state time, which is the consequence of finite-amplitude libration (i.e., the middle panel of Fig. 10). With smaller τ_n/τ_e than 70 the period ratio is significantly smaller than 2, which corresponds to the non-resonant regime. On the other hand, for $\tau_n/\tau_e > 180$,

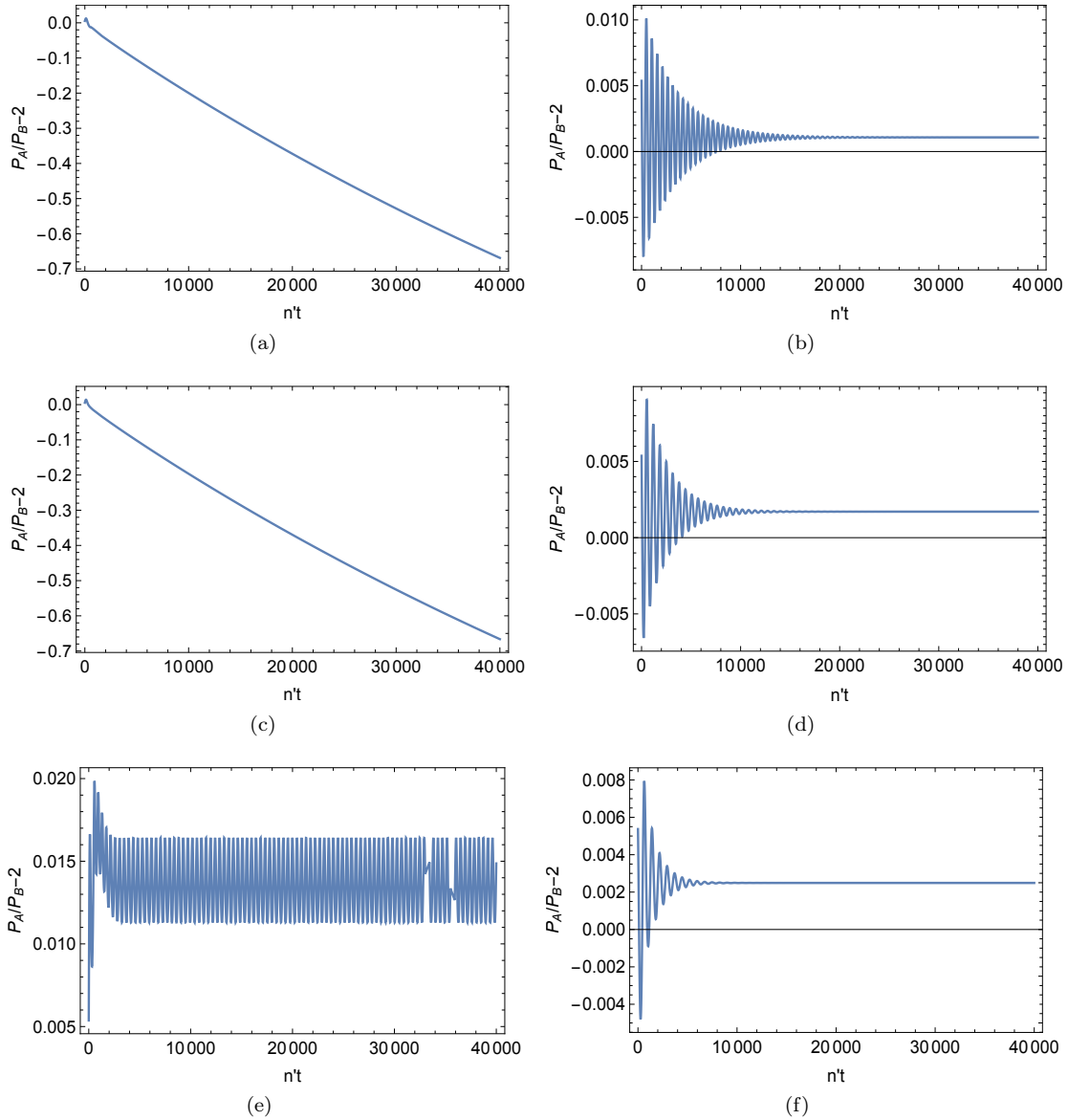


Figure 11. Similar set up as Fig. 10 but with τ_0 set to be $-\tau_n/10$ on the left column and $\tau_n/10$ on the right column.

the period ratio barely oscillates, which corresponds to the fixed point regime.

As the negative τ_0 terms are included, the transition between the non-resonant regime and the libration regime shifts to lower τ_n/τ_e , as we can find for the cases with $\tau_0 = -\tau_n/10, -\tau_n/5$. In addition, as $|1/\tau_0|$ increases, a new non-resonant regime appears in the middle of the regime with roughly constant period ratios, as shown in panel (c,d) of Fig. 12. The presence of additional non-resonant regimes is consistent with our earlier observation that negative τ_0 s tend to drive more system configurations away from the resonant period ratios. On the other hand, for positive τ_0 , i.e., $\tau_0 = \tau_n/10$ as shown in the panel (b), most of the parameter range correspond to a system in resonance locking. Positive τ_0 likely enhances the chance of resonance locking. In summary, the inclusion of τ_0 terms in the evolution equations gives rise to more complex structures in the parameter phase space of such pairs of planets.

5 OBSERVATIONAL IMPLICATIONS

The multi-planet systems discovered that by the *Kepler* mission have shown interesting observational signatures (Fabrycky et al. 2014). First of all, most planets are found to reside away from MMRs. Secondly, for these found trapped in resonances, the period ratios are usually 1%–2% larger than the exact resonance. By introducing the damping terms in the eccentricity and semi-major axis, GS14 manages to explain why it is rare to find planet-pairs trapped in resonances. However, their formalism suggests much smaller offsets (of period ratios) from the exact resonance for these pairs trapped in resonances.

In order to explain the period ratio offset, it was suggested that the tidal damping of eccentricity may play a role (Lithwick & Wu 2012; Batygin & Morbidelli 2013), although Lee et al. (2013) claims that tidal damping cannot account for the measured offsets with reasonable tidal pa-

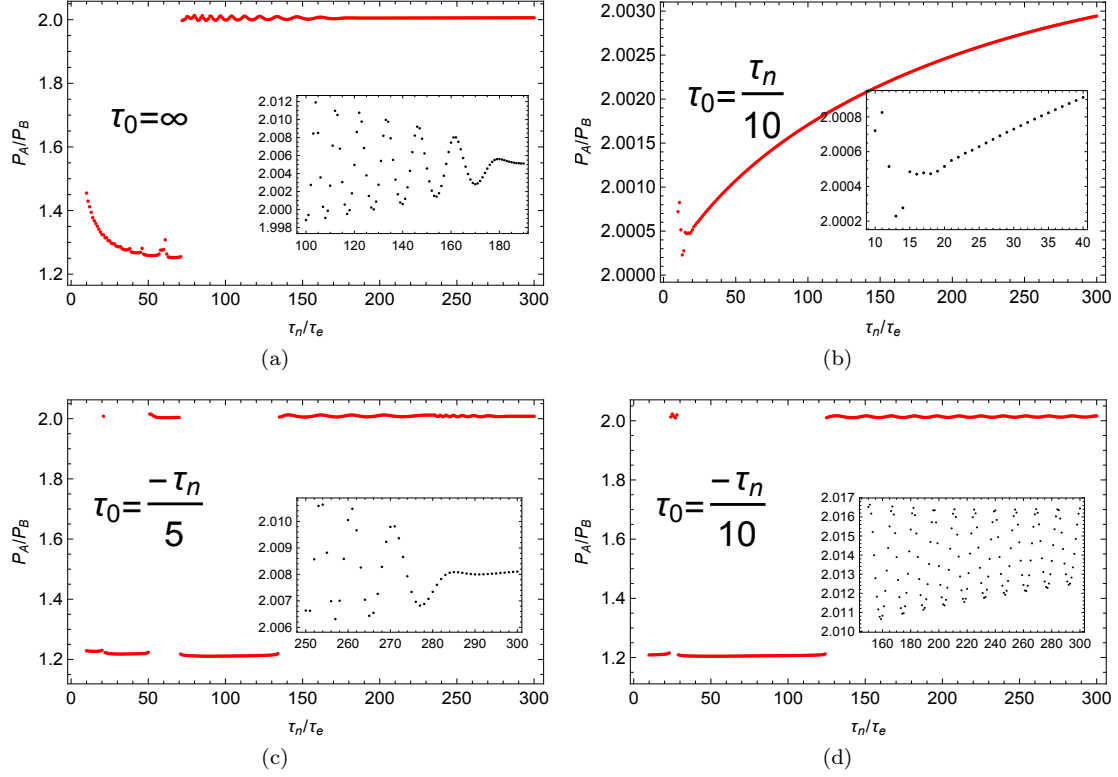


Figure 12. The end state at $n't = 5 \times 10^4$ where the period ratios are extracted for various τ_0 . The inset for each plot provides a zoomed-in illustration for the finite amplitude libration regime and the possible fixed point regime.

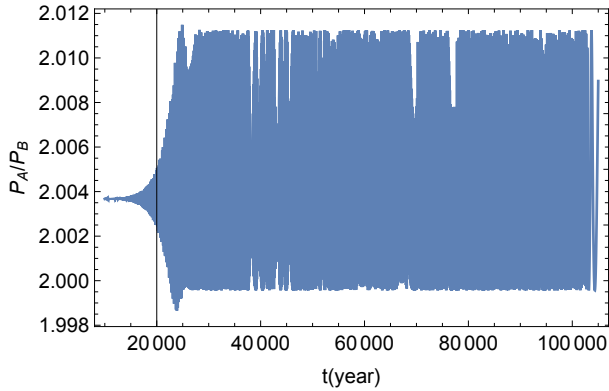


Figure 13. The period ratio of the evolution of a pair of planets with $\mu_B = 0, \mu_A = 10^{-4}$ (with τ_0 terms removed). The damping timescales are assumed to be $\tau_{nA} = 10^5$ years and $\tau_{eB} = \tau_{nA}/100$. The value of τ_{eA} is not important as the eccentricity of object A is negligible in the quasi-stationary state. The system is initially released at $r_A = 0.49$ AU and $r_B = 0.3$ AU, with the star mass being $0.31M_\odot$.

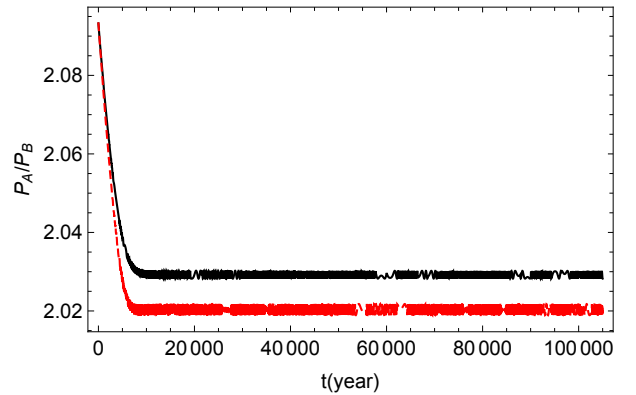


Figure 14. The evolution of a pair of planets with the same system parameters as in Fig. 13, except that the τ_0 terms are turned on. For the red dashed line τ_0 is set to be $-\tau_{nA}/20$ and for the black solid line τ_0 is set to be $-\tau_{nA}/30$.

rameters. On the other hand, the work by Podlowska-Gaca et al. (2012); Baruteau & Papaloizou (2013) suggests that the density waves from the companion damped around the planet may contribute to larger period ratios, which is possibly more efficient if a gap opens by the planet. In this section we investigate the effect coming from interfering density waves, without introducing extra dissipation mechanisms.

We extend the formalism discussed in Sec. 4 by including

the dynamical evolution for both the inner and outer objects. The evolution equations are (we are dealing with a 2 : 1

resonance) (GS14)

$$\begin{aligned}
\dot{n}_B &= 1.89\mu_A n_B^2 (1.19e_B \sin \phi_B - 0.428e_A \sin \phi_A) + \frac{n_B}{\tau_{nB}} + \frac{3n_B e_B^2 \delta n_B}{\tau_{eB}} - \frac{9\mu_A e_{B0} n_{B0}^2}{4\omega_0}, \\
&\quad - \frac{6e_B n_B \cos \phi_B}{\tau_0}, \\
\dot{n}_A &= -6\mu_B n_A^2 (1.19e_B \sin \phi_B - 0.428e_A \sin \phi_A) + \frac{n_A}{\tau_{nA}} + \frac{3n_A e_A^2}{\tau_{eA}}, \\
\dot{e}_B &= 0.75\mu_A n_B \sin \phi_B - \frac{e_B}{\tau_{eB}} - \frac{\cos \phi_B}{\tau_0}, \\
\dot{e}_A &= -0.428\mu_B n_A \sin \phi_A - \frac{e_A}{\tau_{eA}}, \\
\dot{\varpi}_B &= -0.75\mu_A n_B \frac{\cos \phi_B}{e_B}, \\
\dot{\varpi}_A &= 0.428\mu_B n_A \frac{\cos \phi_A}{e_A}
\end{aligned} \tag{59}$$

with $\phi_{A,B} := \vartheta - \varpi_{A,B} := 2\lambda_A - \lambda_B - \varpi_{A,B}$. Notice that in Eq. (59) we have only included the interfering density wave term τ_0 for the evolution equations of object B for simplicity. This is a good approximation as later on we shall focus on the limit that $\mu_A \gg \mu_B$. In addition, the evolution equation for ϑ is

$$\dot{\vartheta} = 2n_A - n_B, \tag{60}$$

which together with Eq. (59) provide seven evolution equations for seven variables $n_A, n_B, e_A, e_B, \varpi_A, \varpi_B, \vartheta$. Let us now consider the case with $\mu_A \gg \mu_B$ discussed in GS14. By setting $\mu_B = 0, \mu_A = 4 \times 10^{-4}$ and $\tau_{eB}/\tau_{nA} = 0.022$, the period ratio can reach a level $\sim 1.5\%$. However, most of the *Kepler* pairs near the 2 : 1 resonance has μ_A being much smaller than 4×10^{-4} , so that it was conjectured that additional eccentricity damping mechanism may be in operation.

In Fig. 13 we are presenting an evolution using Eq. (59) and Eq. (60) (but with τ_0 terms removed) similar to Fig. 12 of GS14. The μ_A is assumed to be 10^{-4} , which is a factor of four smaller than the value used in GS14, and τ_{eB} is set to be $\tau_{nA}/100$. In the stationary state the system undergoes large amplitude librations, with the average period ratio offsets from 2 by about 0.3%, which is clearly much smaller than *Kepler* observations. This is consistent with the findings in GS14, that μ_A has to be set with values higher than those observed in order to explain the 1% – 2% period ratio offsets.

In Fig. 14 we present the evolution of planet pairs with interfering density wave terms included. We find that with $\tau_0 \sim -\tau_{nA}/30$ is the ratio offset can achieve the 1.5% level without the requirement of increasing the mass μ_A . This τ_0 corresponds to

$$\frac{1}{|\tau_0 \beta_0 \mu' n|} \approx 0.18, \tag{61}$$

so that the equivalent force coming from interfering density waves is about 20% of the mutual gravitational interaction for the resonant dynamics. The quasi-stationary part of Fig. 14 can be understood as follows. This state is similar to the rotational state as depicted by the red and black trajectory in Fig. 9(d), although here the rotation amplitude is stationary due to the contribution from both τ_0 and τ_{eB} related terms. If we follow the expansion in Eq. (51) for n_B and e_B , we find that the unperturbed trajectory (without the $\tau_{eB}, \tau_{nA}, \tau_0$

terms) leads to

$$\begin{aligned}
\dot{n}_B &= -\frac{9\mu_A e_{B0} n_{B0}^2}{4\omega_0}, \\
\dot{e}_B &= -\frac{3\mu_A n_{B0}}{4\omega_0}
\end{aligned} \tag{62}$$

where $\omega_0 = 2n_A - n_{B0}$. The corresponding conserved quantity k for this system is given by

$$k = \frac{3e_B^2}{2} - \frac{3\mu_A \cos \phi_B}{4e_B} + \frac{\dot{Q}}{n_B}. \tag{63}$$

Now we treat the terms associated with $\tau_0, \tau_{eB}, \tau_{eA}$ as perturbations, and find that

$$\dot{k} = 3e_B \dot{e}_B + \frac{2\dot{n}_A}{n_B} - \frac{\dot{n}_B}{n_B} = -\frac{6e_B^2}{\tau_{eB}} + \frac{3e_B \cos Q}{\tau_0} + \frac{1}{\tau_{nA}}. \tag{64}$$

The stationary state requires that the time average of \dot{k} is zero, i.e., $\langle \dot{k} \rangle = 0$, which leads to

$$\frac{1}{\tau_{nA}} - \frac{6e_{B0}^2}{\tau_{eB}} - \frac{9\mu_A n_{B0}}{4\tau_0 \omega_0} \left(1 + \frac{3n_{B0} e_{B0}^2}{2\omega_0} \right) = 0. \tag{65}$$

Dropping the subdominant term in the bracket we obtain the period ratio offset as

$$\left\langle \frac{2n_A}{n_B} - 1 \right\rangle = \frac{\omega_0}{n_{B0}} \approx \frac{9\mu_A \tau_{nA}}{4 \tau_0} \left(1 - \frac{6e_{B0}^2 \tau_{nA}}{\tau_{eB}} \right)^{-1} \tag{66}$$

which is approximately -1.5% for $\tau_0 = -\tau_{nA}/30$ (in the asymptotic state $e_{B0} \sim 0.03$), agreeing well with the numerical evolution. It is evident that strong torque from the interfering density waves would lead to larger period offset. It is also possible that the interfering density waves provide the eccentricity damping mechanism to allow large period ratio offsets as observed in *Kepler* multi-planet systems.

6 CONCLUSION

In this work we have discussed a new type of disc-mass interactions for a pair of point masses moving within an accretion disc. When the orbital phases of the masses are locked into a nearly constant resonant angle, the interfering density waves produce an extra piece of angular momentum flux that does not average to zero over orbital timescales. Using a two-dimensional theory with the same vertical averaging scheme in W88, we compute the backreaction of the disc on to the planets near an MMR. We find that the backreaction torque is mainly contributed by the disc materials around the Lindblad resonance location close to one of the planets. The excitation amplitude Ψ blows up for a standard two-dimensional theory but can be regularized by various smoothing schemes, e.g., the one discussed in W88. For the particular 2 : 1 inner resonance we compute the relevant torque acting on the inner planet due to this mechanism.

We have designed a set of hydrodynamical simulations to verify the analytical predictions. The simulations are also intrinsically two-dimensional, so that another smoothing scale ϵ is introduced in the gravitational potential following common practise in the literature of disc simulations. Interestingly, the analytical theory with this smoothing scheme predicts a different torque. We perform a first simulation with a pair of planets following prescribed motion either in the 2:1 and 3:2 MMR state or the out-of-resonance state, and measure

the corresponding disc gravitational force on the planets. We also perform separate hydrodynamical simulations with either the outer planet or inner planet alone, but with orbital parameters the same as in the first simulation, and measure the disc backreaction. In this way we can subtract the torques and obtain the additional torque due to the coupling between the inner planet and the density waves generated by the outer planet. We find that indeed the additional torque is mainly produced in the inner Lindblad resonance which is close to the orbit of the inner planet, with total value being $\sim -2.9 \times 10^{-8}$ in code unit. Notice that the analytical theory predicts a negative torque which is roughly consistent with the numerical values. Other signatures of the interference torque, i.e. the radius of location, the eccentricity and mass dependencies, the Q dependence are all consistent with the analytical theory. Because the sign of the torque depends on the smoothing scheme as discussed earlier, it is clear that the actual torque sensitively depends on the detailed three-dimensional gas structure in the co-rotation regime of the inner planet. In the future, we plan to perform a study in the three-dimensional scenario both with the analytical theory and numerical simulations to resolve the discrepancy. We have introduced an effective τ_0 which can be both positive and negative (corresponding to positive and negative torques respectively) in the discussion of orbital dynamics in Sec. 4 and Sec. 5.

With the new torque due to density wave interference, we have analyzed the dynamics of a part of planets within and outside of the resonance regime. We find that positive τ_0 tend to drive more systems into the resonance regime, whereas negative τ_0 more likely drive the systems away from the resonant period ratios. Indeed in *Kepler's* observation most planet pairs are found to be away from the resonant period ratios. [GS14](#) proposed an explanation by introducing dissipation terms in the orbital evolution equations but [Deck & Batygin \(2015\)](#) have pointed out that the model is insufficient to explain the data by considering more general mass ratios. It is therefore interesting to examine whether the interfering density wave effect can explain the large population of off-resonant pairs - an direction to explore in the future ([Ge et al. 2022](#)). On the other hand, we also find that negative τ_0 can lead to a state with stable period ratio with 1% – 2% offset away from the exact resonant values. This is another observation signatures of planet pairs in *Kepler's* data which can not be naturally explained in [GS14](#). Here the interfering density waves provide an promising mechanism to produce relatively large period ratio offsets, but more extensive studies in the relevant parameter space are necessary to test whether it is fully consistent with data.

At this point, it may be interesting to generalize the effect due to interfering density waves to “resonant dissipations” for systems under resonance as density wave emission is one form of dissipation in a resonant process. The essence of this effect is that dissipative mechanisms may dynamically depend on the resonant angle, so that they may introduce non-trivial influence on the resonant dynamics. For example, one may imagine that the tide-driven migration in planet-satellite systems may exhibit similar phenomena. The planet tides excited by the satellites ([Goldreich & Sciama 1965](#)) may coherently interfere with each other to produce additional resonant dissipation. In EMRI systems relevant for space-borne gravitational wave detection, with a single stellar-mass black hole orbiting around a massive black hole an orbital resonance

may still arise because of the beating between different degrees of freedom of the orbit ([Flanagan & Hinderer 2012](#); [Yang & Casals 2017](#); [Bonga et al. 2019](#); [Pan et al. 2023](#)), which have different cyclic frequencies in the strong-gravity regime. The main dissipation mechanism for these systems are gravitational wave radiation. The beating of gravitational waves of different harmonics near the resonance may give rise to an extra resonant dissipation that depends on the resonant angle and modify the resonant dynamics in a nontrivial manner.

ACKNOWLEDGMENTS

We thank Houyi Sun for helpful discussions and the anonymous referee for many constructive comments. H. Y. is supported by the Natural Sciences and Engineering Research Council of Canada and in part by Perimeter Institute for Theoretical Physics. Research at Perimeter Institute is supported in part by the Government of Canada through the Department of Innovation, Science and Economic Development Canada and by the Province of Ontario through the Ministry of Colleges and Universities. Y.P.L. is supported in part by the Natural Science Foundation of China (grant NO. 12373070, and 12192223), and Natural Science Foundation of Shanghai (grant NO. 23ZR1473700). The calculations have made use of the High Performance Computing Resource in the Core Facility for Advanced Research Computing at Shanghai Astronomical Observatory.

DATA AVAILABILITY

The data underlying this article will be shared on reasonable request to the corresponding author.

REFERENCES

- Ansdell M., et al., 2016, *ApJ*, 828, 46
 Baruteau C., Papaloizou J. C. B., 2013, *ApJ*, 778, 7
 Batygin K., Morbidelli A., 2013, *AJ*, 145, 1
 Benítez-Llambay P., Maset F. S., 2016, *ApJS*, 223, 11
 Bonga B., Yang H., Hughes S. A., 2019, *Phys. Rev. Lett.*, 123, 101103
 Dai F., et al., 2024, *arXiv e-prints*, p. [arXiv:2406.06885](#)
 de Val-Borro M., et al., 2006, *MNRAS*, 370, 529
 Deck K. M., Batygin K., 2015, *ApJ*, 810, 119
 DeLaurentiis S., Epstein-Martin M., Haiman Z., 2023, *MNRAS*, 523, 1126
 Dempsey A. M., Li H., Mishra B., Li S., 2022, *ApJ*, 940, 155
 Fabrycky D. C., et al., 2014, *ApJ*, 790, 146
 Flanagan E. E., Hinderer T., 2012, *Phys. Rev. Lett.*, 109, 071102
 Ge J., et al., 2022, *arXiv e-prints*, p. [arXiv:2206.06693](#)
 Goldreich P., Schlichting H. E., 2014, *AJ*, 147, 32
 Goldreich P., Sciama D., 1965, *Monthly Notices of the Royal Astronomical Society*, 130, 159
 Goldreich P. M., Tremaine S., 1979, *ApJ*, 233, 857
 Goldreich P., Tremaine S., 1980, *ApJ*, 241, 425
 Huang S., Ormel C. W., 2023, *MNRAS*, 522, 828
 Kaaz N., Schröder S. L., Andrews J. J., Antoni A., Ramirez-Ruiz E., 2023, *ApJ*, 944, 44
 Kocsis B., Yunes N., Loeb A., 2011, *Phys. Rev. D*, 84, 024032
 Lai D., Muñoz D. J., 2023, *ARA&A*, 61, 517
 Lee M. H., Fabrycky D., Lin D. N. C., 2013, *ApJ*, 774, 52

- Li R., Lai D., 2022, *MNRAS*, **517**, 1602
- Li R., Lai D., 2023, *MNRAS*, **522**, 1881
- Li Y.-P., Dempsey A. M., Li S., Li H., Li J., 2021, *ApJ*, **911**, 124
- Li Y.-P., Dempsey A. M., Li H., Li S., Li J., 2022, *ApJ*, **928**, L19
- Li J., Dempsey A. M., Li H., Lai D., Li S., 2023, *ApJ*, **944**, L42
- Lissauer J. J., et al., 2012, *ApJ*, 750, 112
- Lithwick Y., Wu Y., 2012, *ApJ*, 756, L11
- Murray C. D., Dermott S. F., 2000, *Solar system dynamics*. Cambridge university press
- Pan Z., Yang H., 2021a, *Phys. Rev. D*, 103, 103018
- Pan Z., Yang H., 2021b, *ApJ*, 923, 173
- Pan Z., Lyu Z., Yang H., 2021, *Phys. Rev. D*, 104, 063007
- Pan Z., Yang H., Bernard L., Bonga B., 2023, *Phys. Rev. D*, **108**, 104026
- Peale S. J., 1976, *ARA&A*, 14, 215
- Peng P., Chen X., 2023, *ApJ*, 950, 3
- Petrovich C., Malhotra R., Tremaine S., 2013, *ApJ*, 770, 24
- Podlewska-Gaca E., Papaloizou J. C. B., Szuszkiewicz E., 2012, *MNRAS*, 421, 1736
- Rowan C., Boekholt T., Kocsis B., Haiman Z., 2023, *MNRAS*, **524**, 2770
- Rowan C., Whitehead H., Boekholt T., Kocsis B., Haiman Z., 2024, *MNRAS*, **527**, 10448
- Shakura N. I., Sunyaev R. A., 1973, *A&A*, **500**, 33
- Tanaka H., Ward W. R., 2004, *ApJ*, 602, 388
- Tanaka H., Takeuchi T., Ward W. R., 2002, *ApJ*, 565, 1257
- Wang Y., Zhu Z., Lin D. N. C., 2024, *MNRAS*, **528**, 4958
- Ward W. R., 1988, *Icarus*, 73, 330
- Weiss L. M., Millholland S. C., Petigura E. A., Adams F. C., Batygin K., Bloch A. M., Mordasini C., 2022, *arXiv e-prints*, p. arXiv:2203.10076
- Whitehead H., Rowan C., Boekholt T., Kocsis B., 2024, *MNRAS*, **531**, 4656
- Yang H., Casals M., 2017, *Phys. Rev. D*, 96, 083015
- Yang H., Bonga B., Peng Z., Li G., 2019, *Phys. Rev. D*, 100, 124056

This paper has been typeset from a $\text{\TeX}/\text{\LaTeX}$ file prepared by the author.